



# Fabrication of FeMnSi-based shape memory alloy components with graded-microstructures by laser powder bed fusion

I. Ferretto<sup>a,b</sup>, A. Sharma<sup>a</sup>, D. Kim<sup>c</sup>, N.M. Della Ventura<sup>a,b</sup>, X. Maeder<sup>a</sup>, J. Michler<sup>a</sup>,  
E. Hosseini<sup>a</sup>, W.J. Lee<sup>d</sup>, C. Leinenbach<sup>a,b,\*</sup>

<sup>a</sup> Empa, Swiss Federal Laboratories for Materials Science and Technology, 3603 Thun, Switzerland

<sup>b</sup> École Polytechnique Fédérale de Lausanne (EPFL), Laboratory for Photonic Materials and Characterization, 1015 Lausanne, Switzerland

<sup>c</sup> Dongnam division, Korea Institute of Industrial Technology, 50623 Yangsan, Republic of Korea

<sup>d</sup> School of Material Science and Engineering, Pusan National University 2, Busandaehak-ro 63beon-gil, Geumjeong-gu, Busan 46241, Republic of Korea

## ARTICLE INFO

### Keywords:

Shape memory alloys  
Microstructure control  
Laser powder bed fusion  
Shape memory effect

## ABSTRACT

This work demonstrates the tailoring of the microstructure of two FeMnSi-based shape memory alloys during laser powder bed fusion. Significant variations in the microstructure of the parts can be induced by modifying the scanning speed or the scanning strategy during the process. Specifically, the volume phase fractions, texture, and grain size and morphology change with the applied processing parameters as the thermal history experienced by the material is modified. Additionally, the generally undesired Mn evaporation during laser melting can be deliberately exploited to manipulate the phase composition in the final microstructure. Taking advantage of this, graded-microstructure samples with tailored amounts of the two phases (bcc- $\delta$  and fcc- $\gamma$ ) and distinct microstructure at different locations can be fabricated. A good combination of pronounced shape memory effect and ultrahigh strength can be achieved in this way. The findings of this study offer valuable insights that can drive future research and advancements in additive manufacturing, opening exciting opportunities for the fabrication of multifunctional and high performance materials.

## 1. Introduction

Fe-based shape memory alloys (Fe-SMAs) are special alloys that return to their original configuration after being deformed. The mechanism responsible for the shape recovery is the reversible phase transformation between the fcc- $\gamma$  austenite phase and the hcp- $\epsilon$  martensite phase [1]. When a load is applied, the fcc- $\gamma$  austenite partially transforms to hcp- $\epsilon$  martensite. The latter changes back to the austenite phase if heating is applied. In this way, the shape memory effect (SME) is activated, and the SMAs can partially recover their original shape [2]. A partial recovery of deformation already takes place when the load is removed because of the so called material's pseudo-elasticity (PE). The extent of recoverability strongly depends on microstructural features, such as volume phase fractions (fcc- $\gamma$  and bcc- $\delta$  phases) [3], grain size [4], and crystallographic texture [5,6].

Laser powder bed fusion (LPBF) is an additive manufacturing (AM) technique that allows for the manipulation of the microstructure of the fabricated parts. By changing the LPBF process parameters, components with varying microstructures can be manufactured, as the thermal

history experienced by the material during deposition can be site-specifically modified [7,8]. The solidification mode of the material can be controlled by varying laser parameters (e.g., laser power, scanning speed) [9] and scanning patterns [10]. With this approach, it becomes feasible to effectively adjust the crystallographic texture, as well as the grain size and morphology of various alloy categories, such as stainless steels and Ni-alloys, both in the LPBF process and in electron beam melting (EBM) techniques [11–17]. This development opens up new possibilities for deliberate microstructural engineering, facilitating the manufacturing of customized components with distinct microstructures (and consequently, unique properties) in different regions across the sample [9]. By changing the scanning strategy, for example, equiaxed solidification only in certain regions of a Ni-alloy sample could be introduced [18]. With the variation in the laser scanning angle during the process, stainless steel samples with areas displaying distinct textures could be manufactured [12]. Arabi-Hashemi et al. demonstrated that site-specific modifications of the LPBF parameters (i.e. Volumetric Energy Density, VED) can selectively stabilize the ferromagnetic bcc phase while suppressing the paramagnetic fcc phase through controlled

\* Corresponding author at: Empa, Swiss Federal Laboratories for Materials Science and Technology, 3603 Thun, Switzerland.

E-mail address: [christian.leinenbach@empa.ch](mailto:christian.leinenbach@empa.ch) (C. Leinenbach).

<https://doi.org/10.1016/j.addma.2023.103835>

Received 15 June 2023; Received in revised form 30 September 2023; Accepted 16 October 2023

Available online 17 October 2023

2214-8604/© 2023 The Author(s). Published by Elsevier B.V. This is an open access article under the CC BY license (<http://creativecommons.org/licenses/by/4.0/>).

evaporation of nitrogen in selected places of high-nitrogen steel parts [19].

In the context of SMAs, it has been observed that the microstructure of LPBF-manufactured parts and the resulting shape memory properties are rather sensitive to the applied processing conditions. Several studies on Ni-Ti SMAs show the potential of LPBF for controlling chemical composition and transformation temperatures of this alloy system [20, 21]. Modifications of processing parameters affect the amount of Ni evaporation, size and density of precipitates, and grain size. As these microstructural factors have a direct impact on the transformation temperatures of the material, LPBF parameters can be utilized to tune the shape memory properties of Ni-Ti parts based on the desired applications [22,23].

Contrary to the Ni-Ti alloys, the effect of laser parameters on the microstructure of LPBF-fabricated Fe-SMAs has been only scarcely studied until now. The work in [24] points out that the microstructure evolution upon processing of a Fe-Mn-Al-Si SMA is strongly affected by specimen geometry and laser parameters. Significant changes in the microstructure with variation of bar size has been demonstrated, showing a drastic transition from a fine-grained to a strongly-textured columnar-grained microstructure with increasing bar diameter. Recent papers investigate the microstructure modifications introduced by varying VED during LPBF of Fe-Mn-Si-based SMAs [5,25]. For the Fe-17Mn-5Si-10Cr-4Ni SMA [5], a significant reduction in ferrite content and grain refinement are induced by the use of high VEDs. The generated (almost) fully austenitic microstructure leads to a better combination of pronounced ductility, high strength and large recovery strain compared to parts fabricated with lower VED. The amount and distribution of bcc- $\delta$  ferrite and fcc- $\gamma$  austenite of a similar alloy but containing V and C (Fe-17Mn-5Si-9Cr-5Ni-(V,C)) could also be modified by varying the scanning speed during the LPBF process, affecting the components' performance [3].

The present work is a continuation and an extension of these previous studies. The possibility of applying LPBF for the microstructure manipulation in the two SMAs, Fe-17Mn-5Si-10Cr-4Ni and Fe-17Mn-5Si-10Cr-4Ni-(V,C), is systematically explored with regard to the fabrication of graded-microstructure components. Site-specific modifications of the scan velocity as well as rescanning strategies are applied to introduce local variations in the microstructure of the LPBF parts by controlling the evaporation of the volatile element Mn and the solidification conditions during the process. This approach allows for the optimization of material properties, achieving an excellent combination of strength and shape memory properties. As a result, the overall performance of the parts is enhanced, leading to improved functionality and reliability. Additionally, this strategy of site-specific microstructure control paves the way to the production of novel complex geometries with customized material properties, offering opportunities for innovation and advancement across industries such as aerospace, automotive, and healthcare, and fostering the development of advanced materials with unique characteristics and tailored properties.

## 2. Materials and methods

### 2.1. Sample preparation

In this work, two different Fe-Mn-Si-based SMAs are studied. The first investigated alloy, designated as A1, is the same SMA as in the previous studies (all values in wt%: Mn 17.0, Cr 9.9, Si 4.6, Ni 4.6) [5, 26]. The powder particles are generally spherical (Figure A1-a in Appendix A), with a median particle size ( $d_{50}$ ) of 29.7  $\mu\text{m}$  and a size distribution ranging from 10  $\mu\text{m}$  to 50  $\mu\text{m}$ .

The second alloy investigated has a similar composition of A1 but also contains V and C (all values in wt%: Mn 17.8, Cr 10.6, Si 4.8, Ni 4.2, V 0.7, C 0.2). Here, V and C are added to induce carbide precipitation upon aging, which can significantly improve the strength and pseudo-elastic properties of the material [27]. This second powder (A2) has

spherical particles, with some satellites on the surfaces. The powder particles have a  $d_{50}$  of 33  $\mu\text{m}$ . The particle size is between 22  $\mu\text{m}$  and 48  $\mu\text{m}$  (Figure A1-b in Appendix A). Both powders were produced by gas atomization in Argon atmosphere (Metal Player Co., Ltd., Republic of Korea, for A1, and voestalpine BÖHLER Edelstahl GmbH & Co KG, for A2). According to the powder specifications provided by the manufacturers, the alloys contained impurities such as P, S and N in quantities < 0.01 wt%, while the amount of O and H has not been determined.

In a first step, simple cubes (10 mm<sup>3</sup>) were fabricated using a wide range of processing parameters. The samples were produced within an Argon atmosphere (with Oxygen content below 0.1%) utilizing a Sisma MySint 100 additive manufacturing system (Sisma S.p.A., Italy) operating in continuous mode. The system employed a 200 W 1070 nm fiber laser with a Gaussian intensity distribution, resulting in a spot size of 55  $\mu\text{m}$ . The VED (Volumetric Energy Density), which ranges between 72 J/mm<sup>3</sup> and 583 J/mm<sup>3</sup>, is defined as:

$$VED = \frac{P}{v * h * t} \quad (1)$$

where  $P$  indicates the laser power,  $v$  the scanning speed,  $h$  the hatch distance, and  $t$  the layer thickness. To achieve different values of VED,  $P$  (between 130 W and 175 W) and  $v$  (between 100 mm/s and 600 mm/s) were changed, whereas  $h$  and  $t$  were set at 0.1 mm and 0.03 mm, respectively.

Another set of cubic samples was fabricated using rescanning. With rescanning, the already solidified layer is scanned again by the laser before depositing the next powder layer [18]. The first and second scans were performed using different scanning speeds, whereas the power was kept constant at 175 W. The scanning speeds applied range from 100 mm/s to 600 mm/s.

Finally, two different approaches have been adopted to produce functionally-graded samples with spatially varying microstructures. The first consisted in locally modifying the scanning speed in different areas of the samples. The second focused on the rescanning strategy. Once the laser completely scanned the powder layer for the first time, some specific regions of the layer were scanned for a second time.

### 2.2. Microstructure characterization

The manufactured samples were cut along the build direction (BD) for cross-sectional examinations. To prepare the cross section for microstructure analysis, a sequence of grinding steps was performed using SiC paper with grit sizes of 600, 1200, 2500, and 4000. For the final polishing, colloidal silica with a particle size of 50 nm was used. The microstructure of the samples was evaluated through optical microscopy (OM) utilizing a Zeiss Axiovert 100 A microscope coupled with a Canon DSLR camera. Electron backscatter diffraction (EBSD) data were collected using a Tescan Mira scanning electron microscope (SEM) equipped with an EDAX DigiView camera and processed with the EDAX OIM Analysis 7.3 software. The EBSD analysis aimed to investigate volume phase fractions, grain size, and texture in different areas of the samples. The chemical composition of the parts was determined by energy-dispersive X-ray (EDX) using the SEM Tescan Mira equipped with an EDAX Octan plus 30 mm<sup>2</sup> EDS detector. Magnetic induction measurements using the feriscope FMP30C were utilized to (semi) quantify the amount of the ferrite phase bcc- $\delta$  in the samples [28].

### 2.3. Characterization of mechanical and shape memory properties

A few samples were selected to investigate the mechanical and shape memory properties by compression uniaxial test of cylindrical samples with an Electromechanical Central Spindle testing machine [LFMZ-50-HM]. The samples were pre-strained to 2% with a deformation rate of 0.2 mm/min. Following the unloading process, the samples were subjected to a thermal cycle of heating up to 200 °C and then cooling to

room temperature (RT) at 2 °C/min. The strain evolution was monitored throughout the thermal cycle using a side-entry extensometer. The extensometer recorded the final strains at 200 °C ( $\epsilon_{\text{rec},200\text{ °C}}$ ), which were then designated as the recovery strain [29]. As utilized for Ni-Ti-SMAs [30–32] or Fe-SMAs [24], the height-to-diameter ratio of the cylindrical samples is 1.5 (5 mm diameter, 7.5 mm height). Samples were cut by electro-discharge machining (EDM) from blocks (10×6×6 mm<sup>3</sup>) such that the loading direction (LD) of the samples is perpendicular to the BD.

The SME was also characterized in a tensile deformation mode with flat dog-bone shape. Rectangular blocks (63 mm × 20 mm × 20 mm) were fabricated, from which flat tensile dog-bone samples were cut by EDM. The flat samples have a gauge with a width of 1.6 mm, a thickness of 1.5 mm, and a length of 32 mm. The LD of the samples is perpendicular to the BD. Offset yield strengths at 0.1% and 0.2% strain ( $\sigma_{0.1\%}$ ,  $\sigma_{0.2\%}$ ) were measured in a Zwick/Roell Z020 tensile testing machine. The machine has a climate chamber for SME characterization. The strain was recorded by a clip-on extensometer equipped with a thermocouple to measure its temperature during the tests and subsequently compensate for the temperature effect on extensometer readings. After pre-straining to 2% (deformation rate of 0.2 mm/min), the samples were unloaded to a load of 10 N. The samples were heated (200 °C) and cooled, maintaining this load constant. The strain at RT was defined as recovery strain ( $\epsilon_{\text{rec}}$ ).

In addition to the recovery strain, the SME under constraints, i.e., the material's recovery stress, was determined. After pre-straining, the same heating and cooling profile was applied to the samples while the machine crosshead was fixed. The developed stress at RT (after the thermal cycle) was defined as recovery stress,  $\sigma_{\text{rec}}$ . More information about the recovery stress measurements for Fe-Mn-Si SMAs can be found elsewhere [4,33]. Also, the pseudo-elastic strain ( $\epsilon_{\text{pse}}$ ) was calculated from the pre-straining curves as the difference between the strain achieved considering a linear unloading and the effective strain measured upon unloading [34].

Micro-hardness measurements were conducted using a Fischerscope HM2000 microhardness tester to determine the hardness of the fabricated blocks. A load of 300 mN was applied for a duration of 10 s. Hardness measurements were performed in an array of 40 points with 0.1 mm spacing between the points.

### 3. Results

#### 3.1. Microstructure formation

Fig. 1 shows the variation of the amount of bcc- $\delta$  with the VED (Fig. 1-a) and the scanning speed (Fig. 1-b,c) for the samples fabricated from the alloys A1 and A2, measured using the feritscope. A different trend is observed for the two alloys. The amount of ferrite in the A1 samples (Fig. 1-a) decreases with increasing VED until it reaches a

minimum in the ferrite content (below 10%) for a VED of 194 J/mm<sup>3</sup>. At very high VED, the ferrite content starts to increase again and reaches values of more than 90%. From Fig. 1-b, it can be seen that the applied scanning speed plays a key role in the amount of ferrite formation. Independently from the applied laser power, the use of a relatively low scanning speed of 300 mm/s induces a significant reduction in the amount of ferrite (Fig. 1-b). The highest amounts of ferrite are measured in the samples fabricated with a high (600 mm/s) or very low scanning speed (200 mm/s).

A different trend is observed for the A2 samples, for which the amount of ferrite progressively increases with the increase in the VED (Fig. 1-a). The microstructure of the A2 samples fabricated at low VED consists of an almost fully austenitic microstructure (less than 10% of ferrite). The ferrite content slightly increases for the scanning speed of 450 mm/s and 300 mm/s, and increases significantly for the lowest speed of 200 mm/s (Fig. 1-c).

Another important parameter, which affects the microstructure of the fabricated components, is the scanning strategy.

Laser rescanning is normally used to improve the surface quality on the top surfaces and increase the density of the parts [35,36]. Variations in the microstructure, such as grain morphology and grain size, can also be introduced with rescanning [18]. For the rescanned samples in the present work, the laser power was set at 175 W. Considering the strong effect of the scanning velocity on microstructure formation (see Fig. 1-b, c), different scanning speeds for the first scan and the rescanning were tested. The applied scanning speeds range from 100 mm/s to 600 mm/s. Table A1 in Appendix A summarizes the different fabricated samples and the applied scanning speeds. Fig. 2 shows the microstructure of two samples fabricated using the rescanning strategy (Alloy A1). For the first sample, the scanning speeds are 250 mm/s for the first scan and the rescanning. For the second sample, the scanning speed is 400 mm/s for both scans. The EBSD analysis of the other samples fabricated using rescanning is shown in Figure A2 in Appendix A. It is observed that, regardless the applied scanning speeds, rescanning strategy leads to an almost fully ferritic microstructure, with coarse elongated grains with a preferential <001> orientation along the BD. Despite the high heat accumulation caused by rescanning, almost no defects are observed in the microstructure of the rescanning samples (Figure A3 of Appendix A). Only when the scanning speed is drastically reduced for both the first scan and rescanning (250 mm/s) cracking is observed. A few spherical pores form in the rescanned samples probably due to keyholes and/or porosity of the powders (red arrows in Fig. A3) [5,37]. Lack of fusion defects are generated when the high speed of 600 mm/s is applied (Figure A3-b of Appendix A), especially when the alloy A2 is used, due to a lack of proper overlapping of melt pools [38]. However, the use of rescanning seems to eliminate this type of defects (Fig. A3-b).

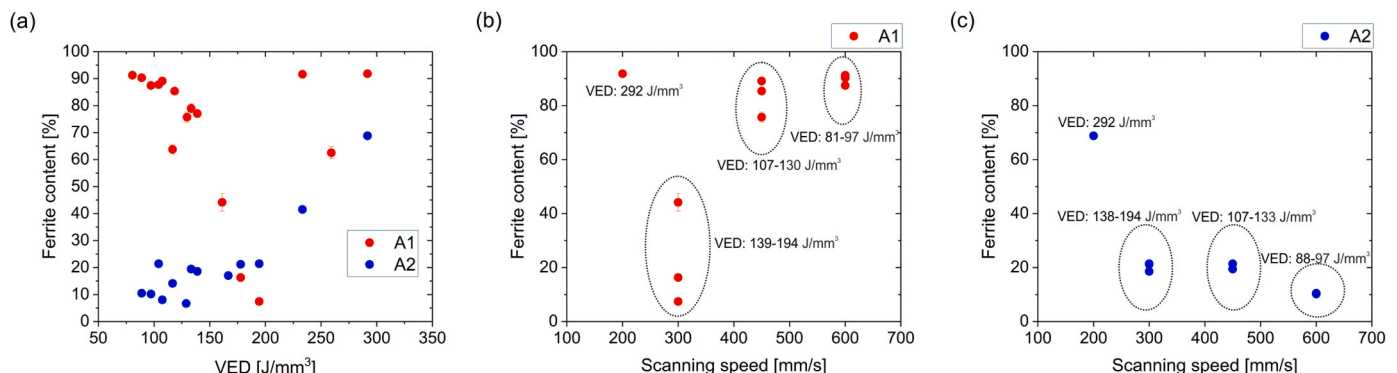


Fig. 1. Variation in the amount of bcc- $\delta$  ferrite in samples fabricated from alloys A1 (red) and A2 (blue) with the VED (a) and with the scanning speed (b,c).

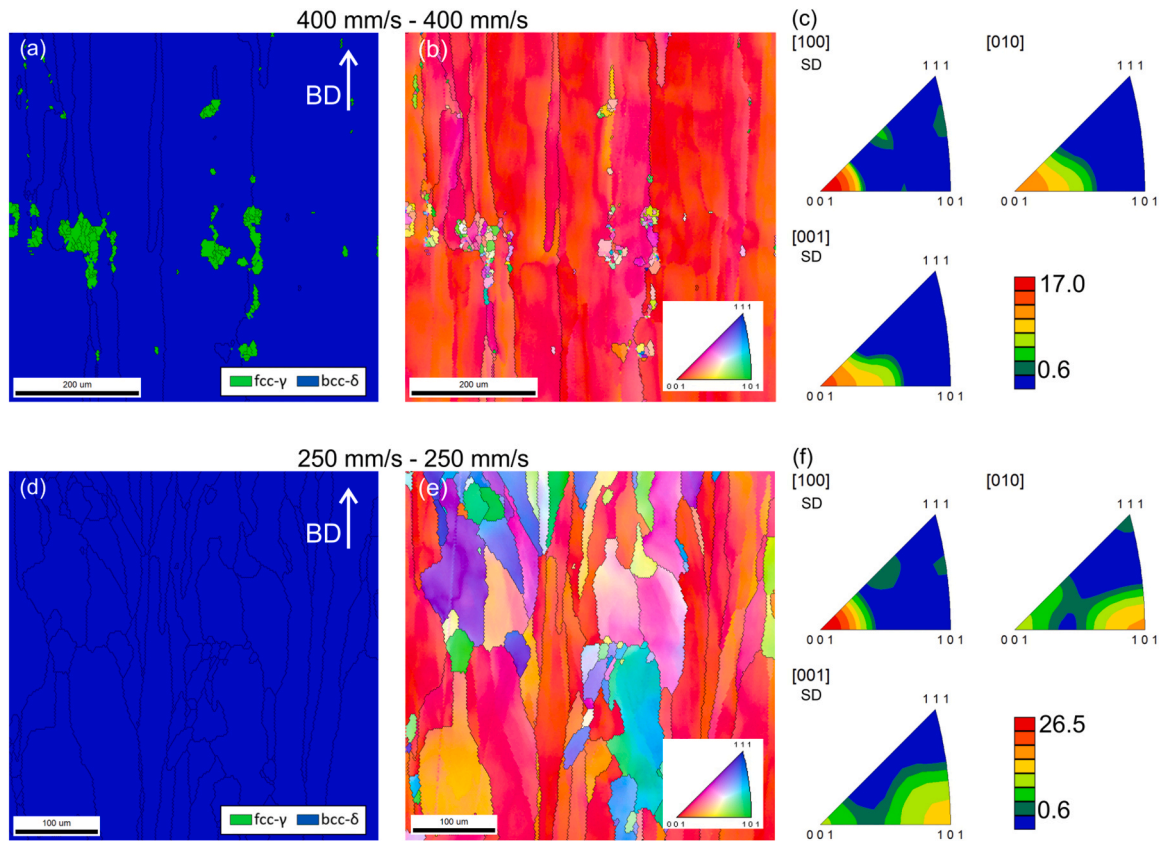


Fig. 2. EBSD maps with phase coloring (a,d), EBSD maps with IPF coloring related to the BD (b,e) and IPFs related to the BD and the two scanning directions (SD) (c, f) of the samples fabricated using rescanning (first and second scans at 250 mm/s and 400 mm/s).

### 3.2. Graded-microstructure samples

The reported examples demonstrate that full control of the phase and microstructure formation could be achieved with these alloys during the LPBF process. Grain size, phase fractions, and texture could be site-specifically modified by tailoring the processing parameters on a local scale, allowing the fabrication of graded-microstructure samples.

A first sample with dimensions of  $4 \times 4 \times 4 \text{ mm}^3$  was fabricated from the alloy A1 by modifying the scan velocity and, therefore, the VED in different areas of the sample (Fig. 3-a).

Simply by changing the scan velocity from 100 mm/s (VED1) to 600 mm/s (VED2) in different regions of the part, a "chess-board" sample with a dual-phase bcc- $\delta$  and fcc- $\gamma$  microstructure could be fabricated. The areas in which the lower scan velocity was applied are characterized by refined austenitic grains with a  $\langle 101 \rangle$  texture. The average grain size is about  $7.5 \pm 3.1 \mu\text{m}$  (Fig. 3-b,d). The austenitic regions are alternated with areas of coarse elongated grains of bcc- $\delta$  ferrite preferentially  $\langle 001 \rangle$  oriented and obtained by reducing the VED (Fig. 3-b,c,d).

Graded-microstructure samples could also be fabricated using alloy A2. Bigger blocks were manufactured to machine compression samples and test their mechanical and shape memory properties (see Section 3.3). The scanning speed was locally changed at different locations of the samples. The fabricated blocks have total dimensions of  $10 \times 6 \times 6 \text{ mm}^3$  and the single regions fabricated at different speeds are 1-mm wide. The scan direction was rotated by  $90^\circ$  between two adjacent regions in order to avoid excessive heat accumulation at the interface. The samples were produced by alternating fast scanning speeds (400 mm/s, Figure A4 in Appendix A, or 600 mm/s, Fig. 4) with a low speed of 100 mm/s in adjacent regions. In every region, the laser power and the hatch spacing were kept constant at 175 W and 0.1 mm, respectively. The layer thickness was set to 0.03 mm. In this way,

layered samples with a clear difference in the phase microstructure of the differently-scanned regions could be fabricated, as shown in Fig. 4 (and Figure A4 in Appendix A). Contrary to the previous sample fabricated from alloy A1, for alloy A2 the reduction in the scanning speed to 100 mm/s causes the formation of ferrite grains that are particularly coarse (average grain size of  $34.0 \pm 10.1 \mu\text{m}$ ), whereas the increase in speed favors the formation of austenite phase (Fig. 4). As can be seen in Table 1 and Fig. 4-c,d, Mn is selectively evaporated in the regions fabricated at high VED, where the amount of Mn reduces below 8 wt%. The amount of the other elements is almost the same in the differently-scanned areas. The areas scanned at 100 mm/s are slightly richer in Fe, Cr, and Ni (Table 1 and Figure A6 in Appendix A). However, the difference in the amount of Fe, Cr, Ni is rather limited compared to the amount of Mn (the amount of Mn reduces to almost half in the 100 mm/s regions). With the high scanning velocity of 600 mm/s (or 400 mm/s), evaporation phenomena are limited or completely avoided (Fig. 4-b). The areas created by higher VED do not have equivalent sizes as initially intended in the CAD input file, where each layer should be 1-mm wide. The coarse ferritic areas are larger, which can be attributed to the larger dimensions of the melt pools associated with high VED [19]. Despite the evaporation of Mn and the use of very low scanning speed, keyhole porosity is rather limited. Only a few pores are observed in the regions scanned at 100 mm/s, as shown in Figure A5-a of Appendix A.

Rescanning was also applied for the fabrication of samples with mixed bcc- $\delta$ /fcc- $\gamma$  microstructure using the alloy A1. "Islands" with different microstructures were introduced within the samples using selective rescanning. For example, as shown in Fig. 5, only the letters "SNF" were scanned a second time after the first laser scan (Fig. 5-a). The laser parameters used for the first and second scans were optimized to avoid excessive heat accumulation within the part that can cause defect formation. Fig. 5 shows the samples fabricated with different scan velocities. The two distinct phases can be identified by OM. The austenite



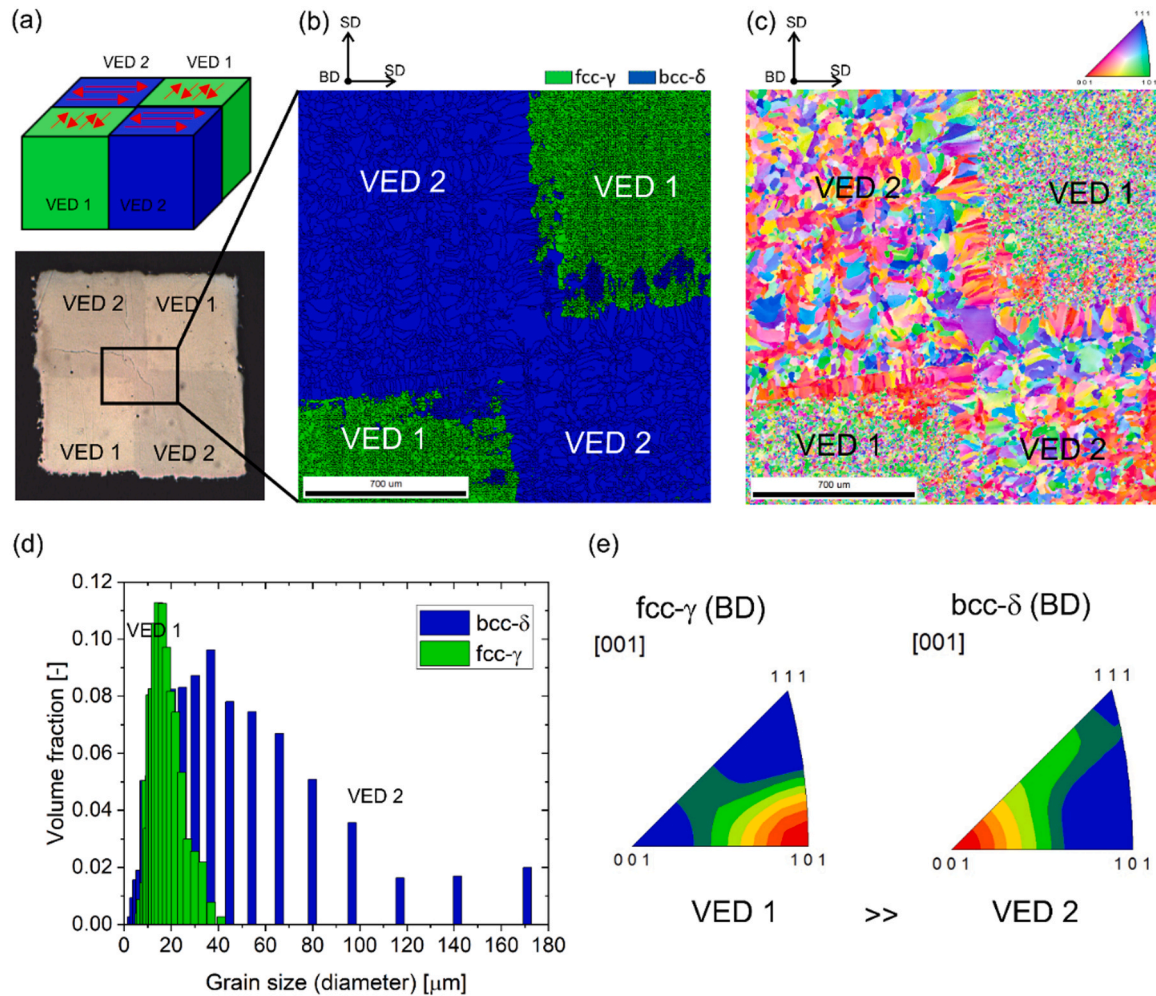


**Fig. 3.** Example of sample with a mixed microstructure; OM image of the top-view of the sample, showing light contrast due to the formation of different phases in different regions of the sample (a); EBSD maps with phase coloring (b) and with IPF coloring related to the BD (c) showing the distinct phase fraction and grain size in differently-scanned areas; grain size distribution (d) and IPFs related to the BD for the fully-austenitic areas (scanned at high VED, VED1) and of the fully-ferritic areas (scanned at low VED, VED 2) (e).

phase appears brighter, whereas the ferrite phase contrasts darkly. When the laser speed is too low in the first scan (i.e., 250 mm/s or 300 mm/s), the rescanned areas show high spherical porosity, presumably due to excessive Mn evaporation. Long cracks also form because of the presence of large regions of brittle ferrite (Fig. 5-b). The best combination of scan velocities was found to be 400 mm/s for the first scan, followed by the second scan performed at 250 mm/s. The as-fabricated sample was investigated via EBSD. For these processing conditions, the fine-grained austenitic microstructure with an average grain size of  $11.0 \pm 4.4 \mu\text{m}$  generated during the first scan at 400 mm/s could be completely transformed into a coarse-grained ferritic microstructure (average grain size of  $49.3 \pm 11.7 \mu\text{m}$ ) in the rescanned area.

Rescanning was also applied for alloy A2 (Fig. 6). The processing parameters, i.e., the scan velocity for the first scan and second scan, were optimized in order to obtain a pronounced difference in the microstructure of the two regions (single-scanned and rescanned) in terms of grain size and bcc-δ/fcc-γ phase fractions. As in the previous case, blocks of 10 mm length and 6 mm height and width were fabricated. With the same applied parameters bigger blocks ( $63 \times 15 \times 15 \text{ mm}^3$ ) were also fabricated to machine dog-bone samples for tensile testing.

Blocks were firstly entirely scanned at a faster speed of 600 mm/s. With this speed, the lowest amount of ferrite is observed in the microstructure and coarse austenite grains form (Fig. 1). However, lack of fusion defects are created (Figure A5-b in Appendix A). Directly after the

first scan, only equidistant narrow regions were rescanned with a scanning speed of 250 mm/s. The width of the rescanned regions was varied for different samples (R-1 mm, R-0.5 mm and R-0.25 mm). For comparison, one sample was fabricated without rescanning and using a speed of 600 mm/s (NO-R sample). Fig. 6 shows the EBSD maps of the three rescanned samples. The rescanned regions are marked with "R" in the images. The resulting microstructure is a dual-phase microstructure, where the austenite grains are relatively refined by the rescanning. Rescanning also eliminates the lack of fusion defects produced by scanning at high speed (Figure A5-b of Appendix A). Some regions of the samples are almost completely free from defects.

The local microstructure modification introduced by rescanning allows for the fabrication of graded samples showing regions of coarser grains of austenite (single-scanned areas) and regions of fine-grained austenite and ferrite (rescanned areas). Position and size of the fine-grained dual-phase areas can be modified as desired, simply by changing the location and the extent of rescanning in the samples. As shown in Fig. 6, in samples R-1 mm and R-0.5 mm, the coarse-grained regions are separated by regions of finer grains of approximately 1 mm or 0.5 mm width, as rescanning was performed for areas 1 mm or 0.5 mm apart. The microstructure of the rescanned samples fabricated with the alloy A2 is characterized by the highest amount of ferrite (about 28%) and the most refined microstructure ( $15.4 \pm 4.2 \mu\text{m}$ ).

It is worth noting that the fine-grained areas are not precisely

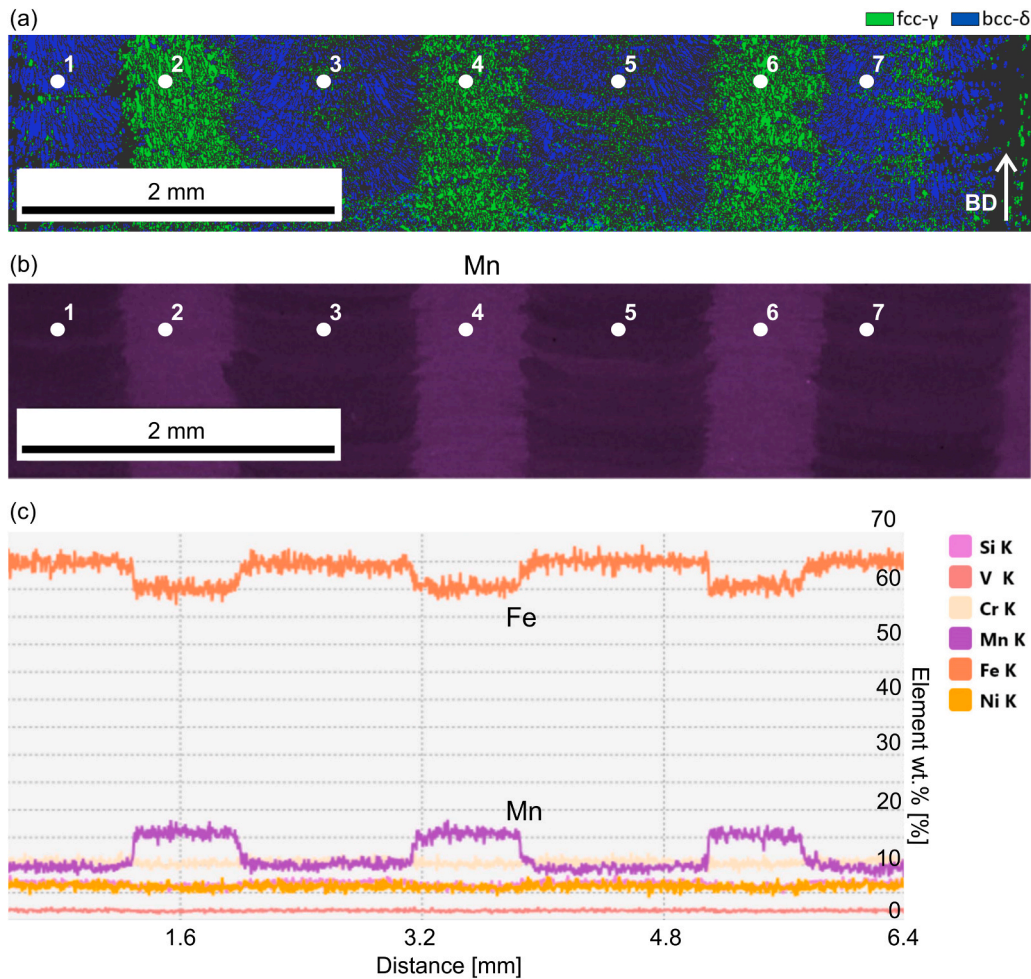


**Fig. 4.** EBSD map with phase coloring of the sample fabricated using the alternation of different scanning speeds, 600 mm/s, and 100 mm/s; EDS map and line scan for determination of chemical composition in the same region of the sample;

**Table 1**

Chemical composition at different locations of the sample fabricated at different scanning speeds of 600 mm/s and 100 mm/s measured by EDS. The point numbers of Fig. 4-c, which indicate the locations where the chemical composition was quantified, and related scanning speed are reported in the table;

Point – scan speed	Fe (wt %)	Mn (wt %)	Si (wt %)	Cr (wt %)	Ni (wt %)	V (wt %)
1 – 100 mm/s	63.9	8.1	10.6	11.1	4.6	1.7
2 – 600 mm/s	59.8	14.8	9.3	10.5	3.9	1.9
3 – 100 mm/s	62.8	7.7	11.8	10.2	6.1	1.5
4 – 600 mm/s	60	13.7	9.3	11.0	4.9	1.2
5 – 100 mm/s	65.6	7.2	10.5	10.7	4.9	1.1
6 – 600 mm/s	60.6	15.1	9.2	10.1	4.0	1.0
7 – 100 mm/s	63.1	8.7	10.5	11.8	4.3	1.6

equivalently sized as planned in the CAD input file. Instead, the created rescanned areas are larger due to the use of the lower speed of 250 mm/s.

### 3.3. Mechanical and shape memory properties

Several functionally-graded samples fabricated using the alloy A2 were selected for compression tests. Fig. 7 shows the shape memory and mechanical properties of the sample fabricated with the alternation of different scanning speeds (400 mm/s and 100 mm/s) from the alloy A2 under uniaxial compressive loading. With this graded-microstructure sample, the most pronounced difference in terms of grain size, texture

and phase fractions has been observed between the differently-scan regions (Figure A4 in Appendix A). The properties of the single-speed scanned samples (400 mm/s only and 100 mm/s only) were also measured and are shown in the graphs for comparison. The stress achieved at 2% strain ( $\sigma_{2\%}$ ) was measured. The yield strength at 0.2% strain could not be accurately determined due to some oscillations in the stress-strain curves at the beginning of the test. The values of  $\sigma_{2\%}$  and  $\varepsilon_{rec,200\text{ }^{\circ}\text{C}}$  are plotted and compared in Fig. 7-c. The sample with a mixed microstructure, which combines mostly austenitic (400 mm/s regions) with mostly ferritic regions (100 mm/s regions), shows a good combination of high strength and pronounced shape memory properties. Compared to the sample scanned at 400 mm/s,  $\sigma_{2\%}$  could be increased by approximately 85 MPa. The recovery strain only slightly reduces compared to the sample fabricated at 400 mm/s (0.71%) and is significantly higher than the one measured for the 100 mm/s sample (0.61% and 0.49%, respectively) (Fig. 7-b).

In order to locally probe the change in the mechanical response, hardness measurements were also performed across the interlayers for the mixed-microstructure sample (Fig. 7-d). A steep gradient in the hardness values is observed between the differently-scanned regions, with a  $\sim 20\%$  reduction in the hardness for the austenitic areas formed from scanning at 400 mm/s.

The mechanical and shape memory properties of the rescanned samples (alloy A2) were also investigated in compression (Fig. 8). Higher stresses are achieved at 2% strain (compression) for the rescanned samples (Fig. 8-a). A slight increase in the stress values is observed for the samples R-1 mm and R-0.5 mm compared to the single-scanned



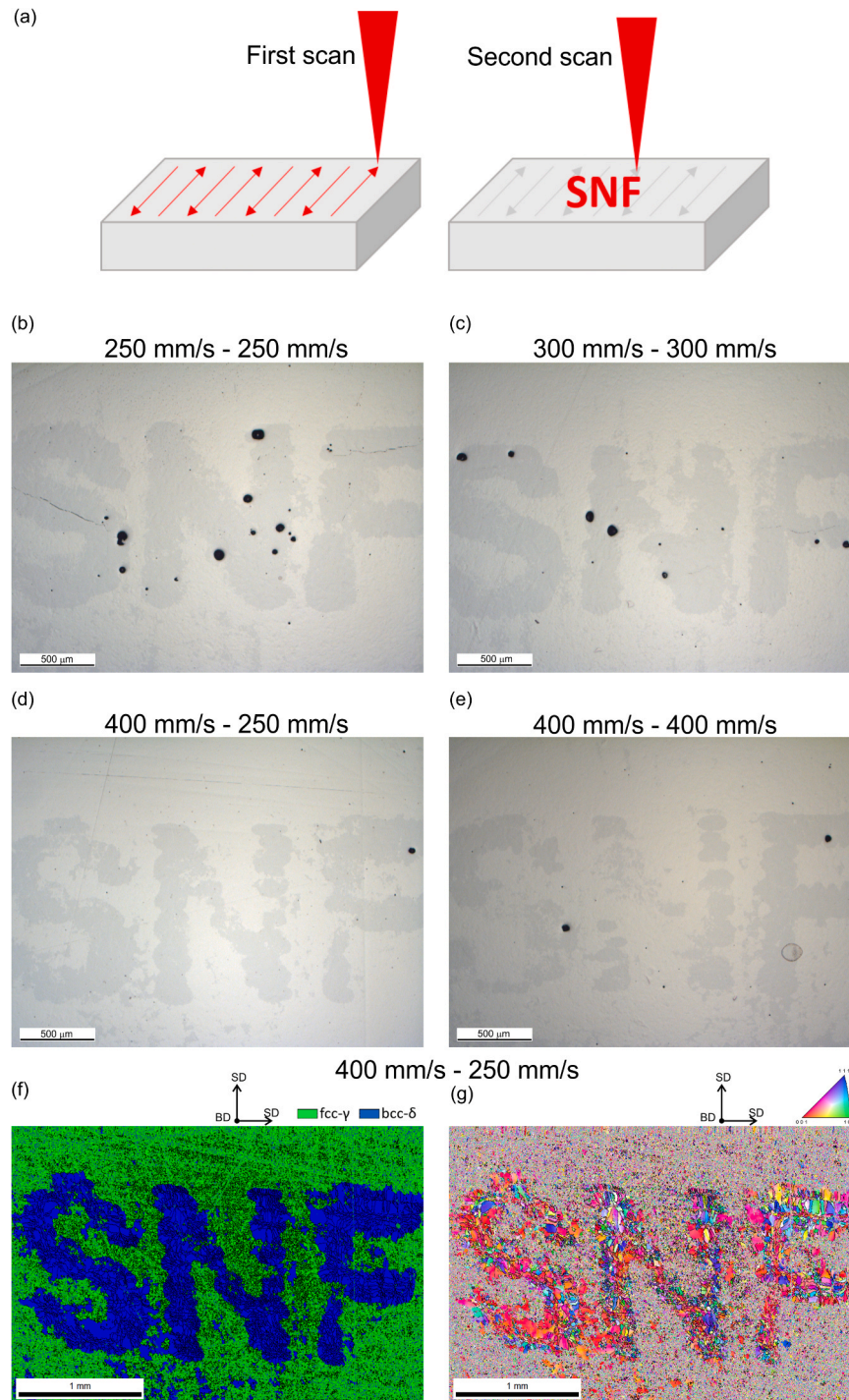


**Fig. 5.** Example of samples with mixed microstructure fabricated using rescanning: only a specific region of the sample ("SNF") is rescanned before depositing new powder (a); OM images of the rescanned samples fabricated using different laser parameters (b,c,d,e); EBSD maps with phase (f) and IPF coloring related to the BD (g) for the sample fabricated using scanning speed of 400 mm/s and 250 mm/s for the first and second scans;

sample, i.e. the sample fabricated without the rescanning (NO-R). The stress at 2% strain becomes more than 40 MPa (R-1 mm) and 20 MPa (R-0.5 mm) higher after rescanning. The improvement becomes significant for the sample R-0.25 mm, for which a stress increase of more than 160 MPa is observed. An opposite trend is observed for the recovery strain (Fig. 8-b,c). The use of rescanning results in a decrease in the recovery strain at 200 °C and RT. During heating to RT after compression deformation, tensile strain develops due to the activation of the SME and the samples' thermal expansion. During cooling to RT, the contraction of the samples due to the thermal effect decreases the

recovery strain. The highest  $\epsilon_{rec,200\text{ }^{\circ}\text{C}}$  is achieved for the NO-R sample, and the lowest for the R-0.25 mm sample.

To confirm the variation in material's performance caused by the microstructure modifications introduced via rescanning, tensile experiments from the rescanned samples were also performed. Tensile samples were fabricated using the same scanning and laser parameters applied for the compression samples. The stress-strain curves during tensile loading to 2%, the recovery strain and recovery stress after 2% pre-straining (tension) and heating to 200 °C, and the pseudo-elastic behavior of the samples were investigated and compared (Fig. 8). The

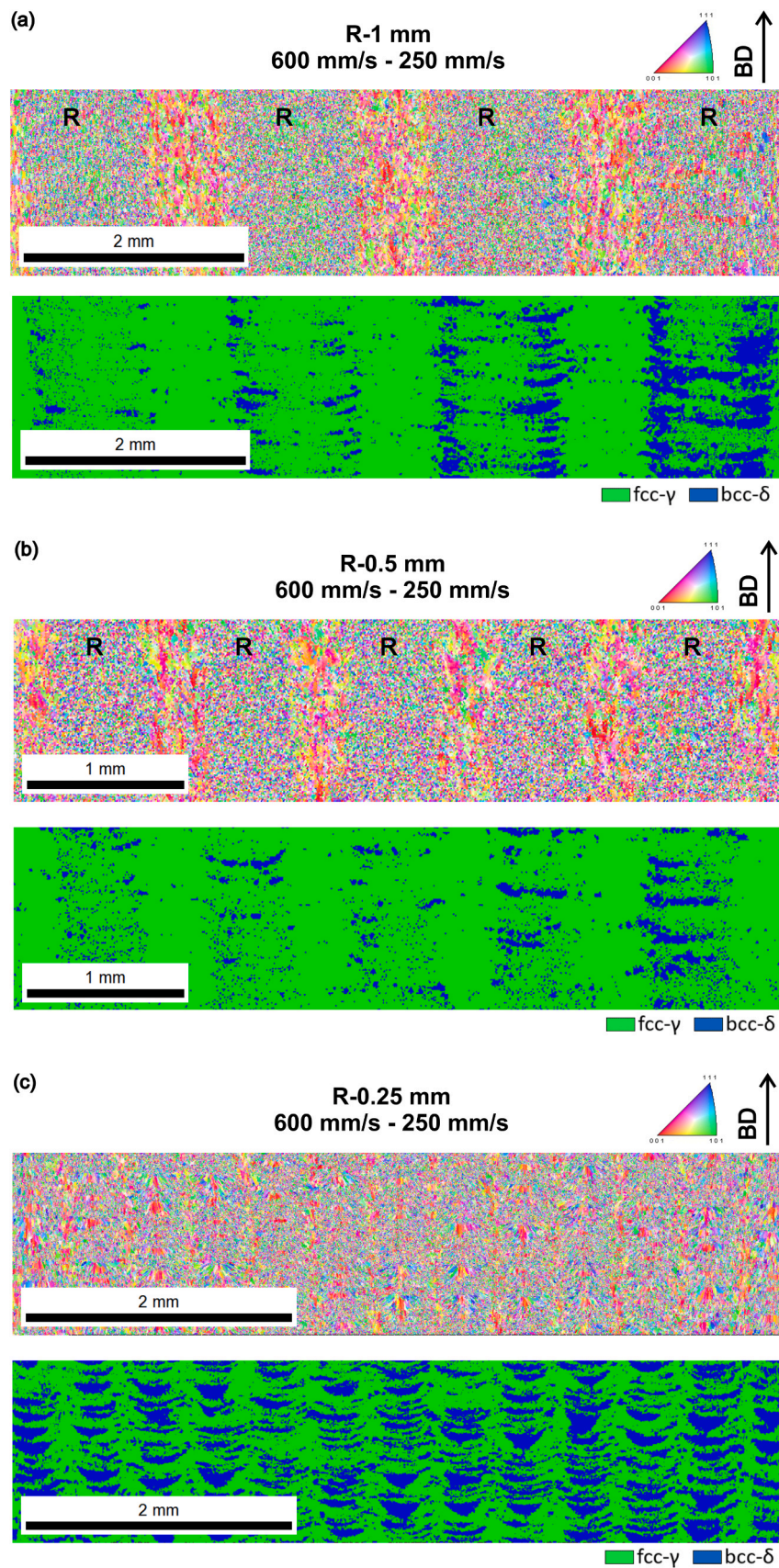


**Fig. 6.** EBSD maps with IPF (related to BD) and phase coloring of the samples fabricated using rescanning (A2 alloy); only layers of the samples of different widths (1 mm (a), 0.5 mm (b), 0.25 mm (c)) are rescanned;



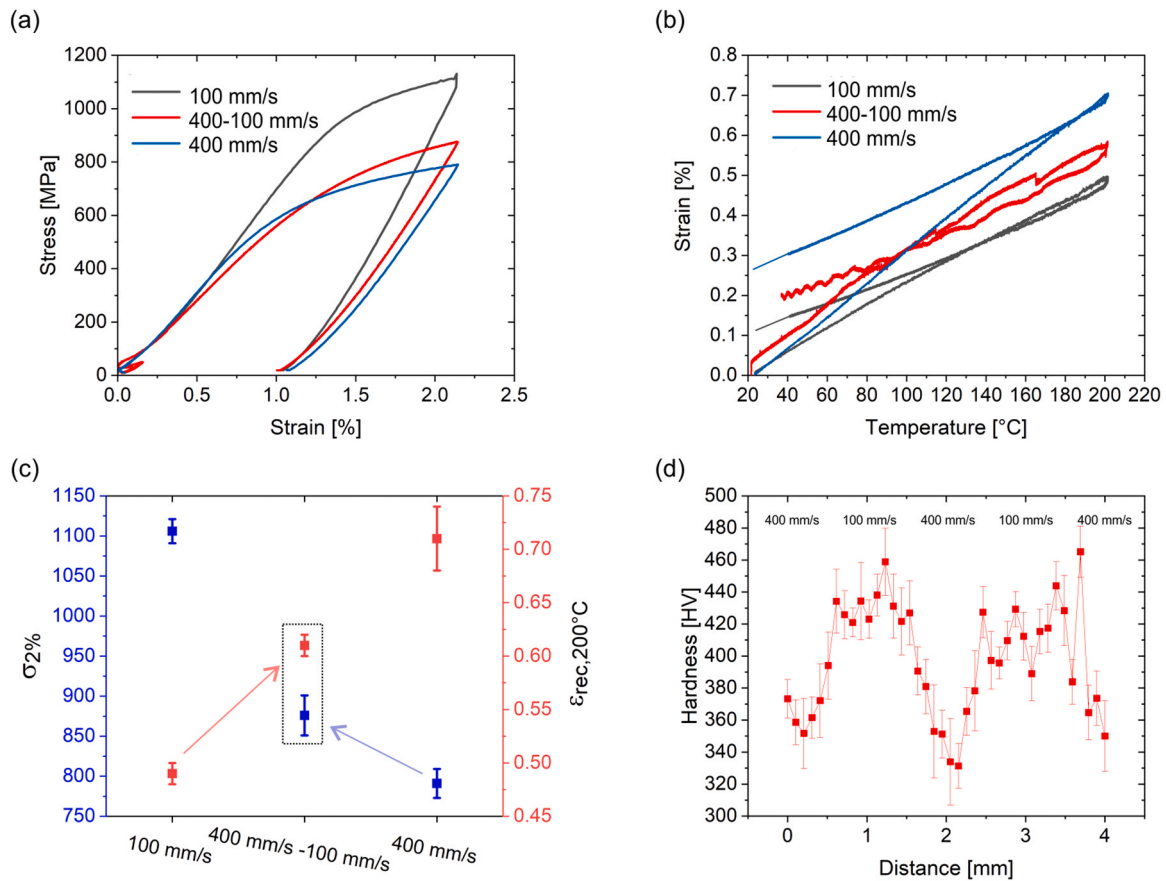


**Fig. 7.** Stress-strain curves during compression up to 2% strain (a) and strain evolution during heating to 200 °C and cooling to RT (after 2% pre-straining) (b) of the samples produced with the low speed of 100 mm/s (black curves), high speed of 400 mm/s (blue curves) and combination of two different speeds (red curves); comparison of the  $\sigma_{2\%}$  and  $\epsilon_{rec,200\text{ }^{\circ}\text{C}}$  values of the three samples (c); hardness values along the sample fabricated using the two different speeds of 400 mm/s and 100 mm/s (d); the tested samples were fabricated using the alloy A2;

obtained trends were very similar to the ones observed during compression loading (Fig. 8-a,b,c). With rescanning, the strength of the material can be improved. The  $\sigma_{0.1\%}$  and  $\sigma_{0.2\%}$  values (Fig. 8-d,g) increase by more than 20 MPa and 30 MPa for the R-1 mm and R-0.5 mm samples compared to the single-scanned one (NO-R). The increase is more than 70 MPa for the R-0.25 mm sample. The evolution of the recovery strain is also similar for tension and compression loading. During heating to 200 °C after the tensile pre-straining, compression strain develops due to the activation of the SME, whereas tensile strain generates from the samples' thermal expansion. The single-scanned sample shows the maximum strain recovery (compression) at 200 °C and RT (Fig. 8-e,h). The SME of the sample counterbalances the effect of thermal expansion. For this reason, almost no sample expansion is recorded up to 200 °C. Contrary, tensile strain is recorded during heating of the rescanned samples, particularly high for the sample R-0.25 mm. During cooling to RT, compression strain further develops due to the samples' thermal contraction. The predominance of the thermal expansion over the SME during heating of the rescanned samples results in the lower recovery strain values recorded at RT (Fig. 8-h, green points). The  $\epsilon_{rec}$  decreases from 0.34% for the NO-R sample to 0.29% for the R-0.25 mm sample.

During constrained heating to 200 °C (Fig. 8-f, recovery stress), the back transformation  $hcp-\epsilon \rightarrow fcc-\gamma$  causes the generation of tensile stress, whereas compression stress develops due to the samples' thermal expansion. For the R-0.25 mm sample, compressive stress is recorded up to 200 °C, indicating that the transformation related stress (tensile) during heating is much smaller than the stress relative to the thermal effect (compressive) (Fig. 8-f, green curve) [4]. The recorded stress at

200 °C is around zero for the R-1 mm and R-0.5 mm samples. The higher SME of these samples compared to the previous case (R-0.25 mm) causes a better balance between the transformation and thermal expansion stress. A tensile stress of about 20 MPa is recorded for the NO-R sample at 200 °C (Fig. 8-f, black curve), confirming the fact that the SME is the highest in the single-scanned sample. During cooling from 200 °C to RT, the recovery stress (tensile) further increases for all samples due to thermal contraction.

A different trend is observed for the pseudo-elastic behavior. PE is rather pronounced ( $\epsilon_{pse}$  of  $0.415 \pm 0.006\%$ ) for the NO-R sample but lower than for the R-1 mm and R-0.5 mm ones. For the latter,  $\epsilon_{pse}$  of  $0.435 \pm 0.004\%$  and  $0.428 \pm 0.004\%$ , respectively, is measured. For the R-0.25 mm sample  $\epsilon_{pse}$  reduces compared to the previous cases.

In Fig. 9, the LPBF-manufactured samples from alloy A2 are compared with previous results from the same alloy but fabricated by conventional routes (hot-rolling). Several studies on aging treatment optimization for conventional SMAs have been performed to improve the mechanical and shape memory properties of the material. As summarized in Fig. 9-a, a simultaneous increase in strength, recovery stress and pseudo-elastic behavior seems not to be possible. For example, aging at high temperatures ( $>700\text{ }^{\circ}\text{C}$ ) leads to relatively low strength and recovery stress ( $\sigma_{0.1\%}$  and  $\sigma_{rec}$  both below 350 MPa), but increased PE (yellow ellipse in the graph of Fig. 9-a). Aging at lower temperature (600–632–700 °C) for very short aging time ( $\leq 4$  h) causes a decrease of both the  $\epsilon_{pse}$  and  $\sigma_{0.1\%}$  (red ellipse). The strength and the recovery stress of the samples increase at the expense of the  $\epsilon_{pse}$ , which reduces to almost half the values achieved for the high-temperature aged samples (light blue ellipse in the graph of Fig. 9-a), if the aging time is prolonged

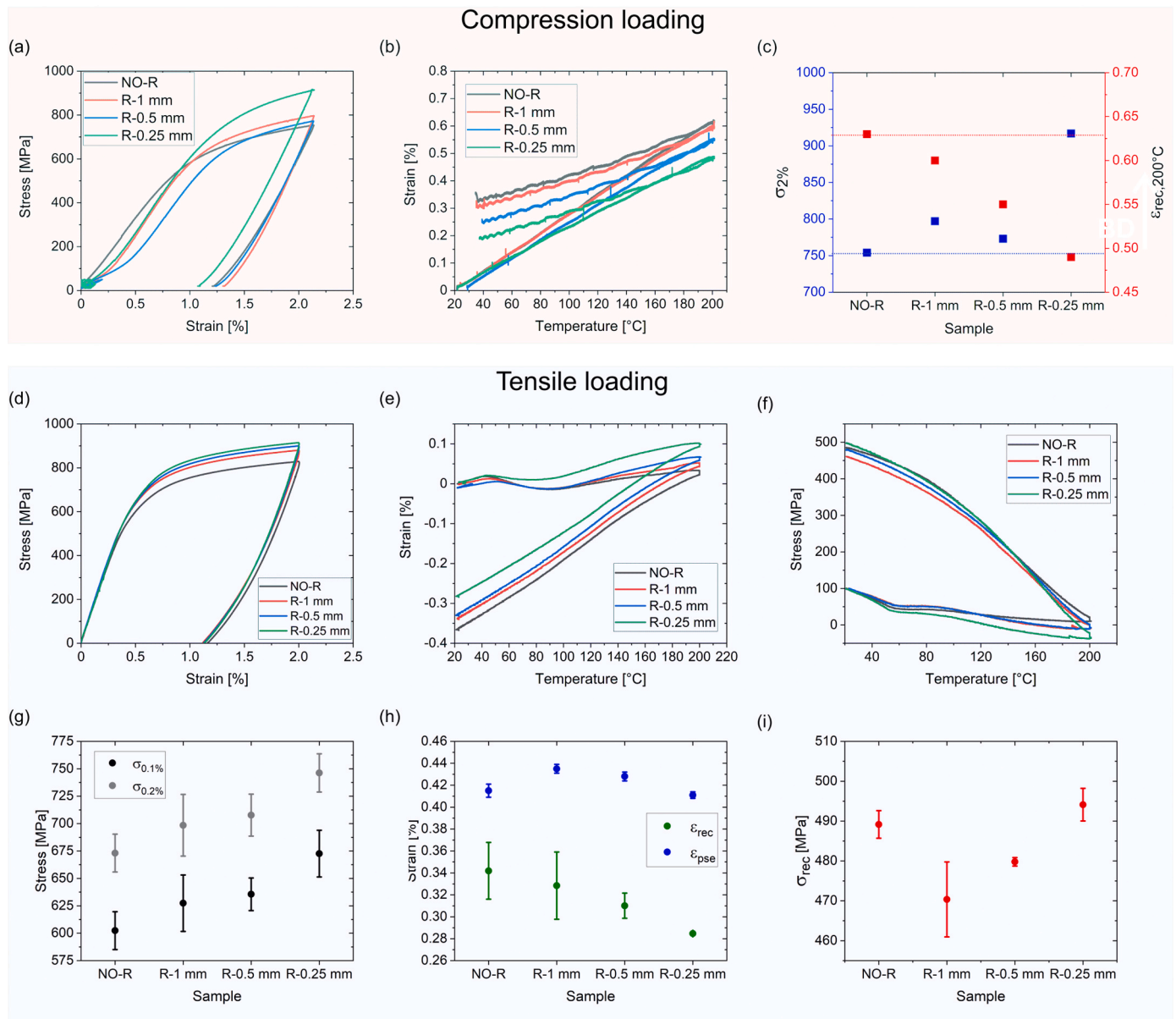


**Fig. 8.** Stress-strain curves during compression loading to 2% (a), evolution of strain as a function of temperature after 2% pre-straining (compression) (b) and  $\sigma_{2\%}$  and  $\epsilon_{rec,200^\circ C}$  values (c) for the samples fabricated at 600 mm/s (NO-R) and with rescanning; stress-strain curves during tensile loading to 2% (d), evolution of strain (e) and stress (f) as a function of temperature after 2% pre-straining (tension) and yield stress (at 0.1% and 0.2%) (g), recovery strain ( $\epsilon_{rec}$ ), pseudo-elastic strain ( $\epsilon_{pse}$ ) (h) and recovery stress ( $\sigma_{rec}$ ) (i) values of the samples fabricated at 600 mm/s (NO-R) and with rescanning; the tested samples were fabricated using the alloy A2;

(between 15 h and 72 h). Only when the aging time is significantly long (in some cases up to 288 h) can relatively high strength and PE be achieved, with values of  $\epsilon_{pse}$  of around 0.25% (dark blue ellipse). Long aging time, however, implies high costs and time of production. The reason for these variations in the thermo-mechanical properties with the aging conditions is found in the different generated microstructure. Size, distribution of precipitates, and SFs density are the main factors that can be modified via the aging treatment and strongly influence the mechanical and shape memory properties of the conventionally fabricated SMA. Detailed information can be found in previous studies [2,4]. From the graph in Fig. 9-a, it is clear that better performance can be achieved with the LPBF-fabricated samples of the present study, which show the best combination of strength, recovery stress and pseudo-elastic behavior. A maximum  $\epsilon_{pse}$  of about 0.29% was obtained in the hot-rolled samples after aging treatment. The average pseudo-elastic strain of the LPBF-fabricated samples is more than 30% higher. The values of  $\sigma_{rec}$  of the LPBF samples are significantly higher, comparable

or slightly lower than for the conventional alloy, depending on the applied aging conditions. The strength ( $\sigma_{0.1\%}$ ) of the LPBF samples could be tuned, i.e. significantly increased, with the use of rescanning. The strength of the LPBF sample fabricated without rescanning is comparable to the strongest conventionally fabricated samples (aged at low temperature for long time). With the rescanning, the  $\sigma_{0.1\%}$  values further increase and exceed the ones of the conventional SMA. The  $\sigma_{0.1\%}$  of the R-0.25 mm rises to 672 MPa. Such high yield strength has never been reported for this specific Fe-Mn-Si alloy system.

In Fig. 9-b, the LPBF-fabricated Fe-17Mn-5Si-10Cr-4Ni(V,C) alloy is compared with other SMA systems produced by casting, hot-rolling, as well as by LPBF, and subjected to specific heat treatments, training, ausforming or thermo-mechanical treatments. Most of the reported data are related to deformation levels between 2% and 4%. Compared to our study, higher activation temperatures have been applied (from 450 °C to 700 °C). The use of higher activation temperatures normally results in higher shape recovery [33]. It is visible from Fig. 9-b that the

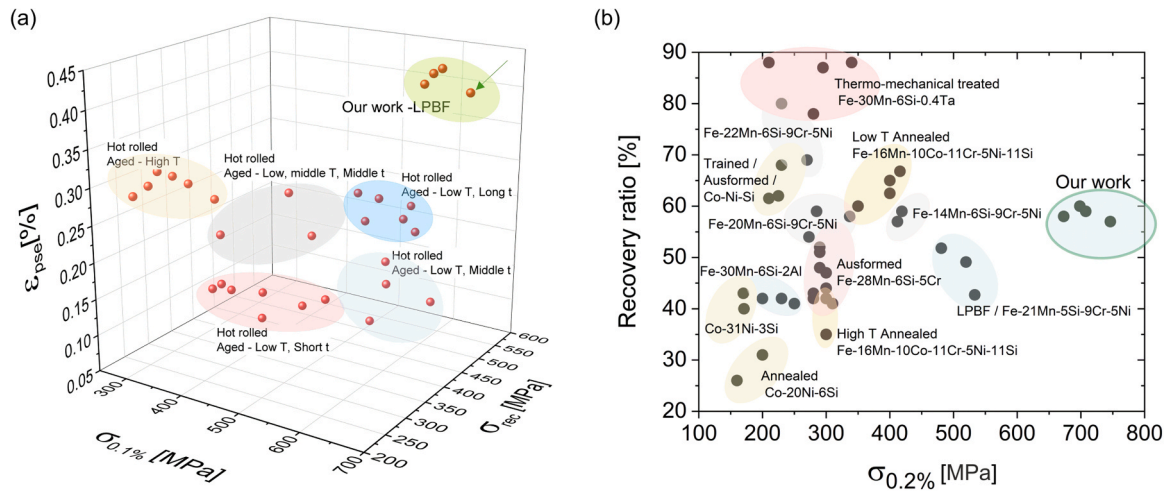


**Fig. 9.** Comparisons of  $\sigma_{0.1\%}$ ,  $\sigma_{rec}$  and  $\epsilon_{pse}$  between the hot-rolled and heat treated Fe-17Mn-5Si-10Cr-4Ni-(V, C) SMA of previous works [2,33,34,40] and the LPBF-fabricated Fe-17Mn-5Si-10Cr-4Ni-(V, C) SMA of the present study (a); comparisons of recovery ratio and  $\sigma_{0.2\%}$  between the previously reported processed and casted Fe-Mn-Si and Co-Ni-Si SMAs and the LPBF-fabricated Fe-17Mn-5Si-10Cr-4Ni-(V, C) SMA of the present study (b);.

polycrystalline Fe-Mn-Si SMAs prepared by casting and then annealed show good strain recovery capability, especially after thermo-mechanical treatments. The recovery ratio, defined as the ratio between the recovered and applied strains, can be increased up to almost 90% [41]. However, the cast polycrystalline Fe-Mn-Si SMAs suffer from poor mechanical properties, probably due to the formation of coarse-grained microstructures. The maximum values of  $\sigma_{0.2\%}$  are around 400–415 MPa [41]. Higher strength is achieved for the Fe-21Mn-5Si-9Cr-5Ni alloy when produced via LPBF. The  $\sigma_{0.2\%}$  increases to about 480 MPa and 530 MPa [25]. These yield stress values are significantly lower if compared with the rescanned samples of the present study. With the extensive rescanning applied for the R-0.25 mm sample, the yield stress at 0.2% strain increases by more than 30%. A recovery ratio of 57% is achieved for the R-0.25 mm and increases up to 60% for the R-1 mm and R-0.5 mm samples. Such recovery properties are comparable or higher than the properties of the Co-Ni-Si SMAs [42] or the cast Fe-Mn-Si SMAs [43], whose recovery ratio can be significantly increased only with special treatments, such as aging, thermal-mechanical treatments, training and ausforming [44–47].

## 4. Discussion

### 4.1. Effect of VED on microstructure formation

It is well reported that the SMAs fabricated by LPBF are characterized by a dual-phase bcc- $\delta$ /fcc- $\gamma$  microstructure [3,48]. As discussed in [5], the solidification microstructure of Fe-Mn-Si-based SMAs is defined by the primary solidification phase and the subsequent solid-state phase transformations [25]. The primary solidification phase can be predicted by empirical formulations (primary phase bcc- $\delta$  ferrite for  $Cr_{eq}/Ni_{eq} > 1.5$  and primary phase fcc- $\gamma$  austenite for  $Cr_{eq}/Ni_{eq} < 1.5$ ) [49,50]. According to these formulations, the alloy A1 of the present study solidifies as bcc- $\delta$  ferrite [25]. The primary bcc- $\delta$  tends to transform to fcc- $\gamma$  during cooling to RT. However, considering the high cooling rates achieved during LPBF ( $10^3$ – $10^8$  K/s) [51], this solid-state phase transformation bcc- $\delta$   $\rightarrow$  fcc- $\gamma$  may be partially or fully suppressed [52–54]. In the LPBF process, the cooling rate experienced by the melt pool and the solidified material depends on the applied processing parameters [55]. When low VEDs are applied and the cooling rate surpasses a specific threshold, the transformation of bcc- $\delta$  to fcc- $\gamma$  is significantly reduced. Instead, the bcc- $\delta$  grains, which are initially grown epitaxially as the primary phase during deposition, do not transform during cooling. As a result, a coarse and predominantly ferritic microstructure is formed, exhibiting a prominent

$\langle 001 \rangle$  texture along the BD (Fig. A7-a). If the VEDs are sufficiently high, the cooling rate decreases and the bcc- $\delta$   $\rightarrow$  fcc- $\gamma$  transformation is no longer inhibited. Kim et al. reported that the transformation of the primary solidification phase is promoted by the so-called intrinsic heat treatment (IHT) [48]. Pre-deposited layers experience cyclic heating during the deposition of the upper layers and the IHT effect becomes more pronounced with increasing VED. For this reason, the amount of austenite within the samples increases significantly at relatively high VED (Fig. 1-a). This solid-state transformation is known to cause pronounced grain refinement [56] and leads to a preferential  $\langle 101 \rangle$  and  $\langle 111 \rangle$  orientation of the austenite grains due to a strict orientation relationship (OR) between the two phases fcc- $\gamma$  and bcc- $\delta$  (Fig. A7-b) [57].

The use of extremely high VED also seems to favor the formation of ferrite in the microstructure (Fig. 1-a). The reason for this increase is found in the significant Mn evaporation induced during LPBF [19,56]. Higher VED implies a greater loss of Mn during the process [58,59]. A reduction of more than 7 wt% of Mn compared to the nominal composition of the powder has been observed with the use of a VED of 583 J/mm<sup>3</sup> [3]. Mn is an austenite stabilizer, so its pronounced evaporation stabilizes the ferrite phase. This prevents the formation of fcc- $\gamma$  during solidification (as a primary solidification phase) and during cooling of the already solidified layers, explaining the further increase in the ferrite content for very high VEDs.

The significant variations in microstructure introduced by changing the processing parameters could be exploited to fabricate the graded-microstructure specimen (paragraph 3.2) with locally tailored, mixed microstructure. For the alloy A1, the areas in which low scan velocities are applied are characterized by refined austenitic grains with  $\langle 101 \rangle$  preferential orientation as the solid-state transformation bcc- $\delta$   $\rightarrow$  fcc- $\gamma$  is promoted by the high temperature and low cooling rate achieved in the pre-solidified layers (Fig. 3) [48,57]. In these locations, the microstructure is refined by the transformation. It is worth mentioning that despite the use of very high VED (583 J/mm<sup>3</sup>), the microstructure is fully austenitic. Due to the reduced size of the sample, the heat accumulation is relatively low and probably not high enough to induce significant Mn evaporation to destabilize the austenitic phase, as it occurs in the bigger cubic samples (Fig. 1). It is known that the size of LPBF samples can significantly influence heat build-up during the process, affecting microstructure and properties of the samples [60]. Computational modeling techniques can simulate the thermal behavior and solidification process during LPBF of different-sized parts, making it possible to predict the microstructure that forms. The austenitic regions

of the graded-microstructure sample are alternated with areas of coarse elongated grains of bcc- $\delta$  ferrite obtained by reducing the VED. The low VED and the induced high cooling rate hinder the transformation of the primary ferrite to austenite. The ferritic phase remains after cooling, maintaining the coarse elongated grains (average grain size of  $45.3 \pm 13.6 \mu\text{m}$ ) with the preferential  $\langle 001 \rangle$  texture along the BD developed during the deposition (Fig. 3-b,c,d,e).

Contrary to samples A1, the lowest amounts of ferrite are measured for the A2 samples when fabricated with the highest scanning speed of 600 mm/s. The alloy A2 has 0.2 wt% of C. Carbon is a strong austenite stabilizer, and small additions of C content can change the primary solidification mode to fcc- $\gamma$  [61]. Indeed, if the powder chemical composition of the alloy A2 is considered, the ratio  $\text{Cr}_{\text{eq}}/\text{Ni}_{\text{eq}}$  is 1.19 [50] or 1.45 [62], indicating that the primary phase is presumably austenite in the alloy A2 and not ferrite as for the alloy A1. The primary austenite that forms for low VEDs shows coarse grains, preferentially  $\langle 001 \rangle$  oriented along BD (Figure A7-c in Appendix A) [37]. When VED increases ( $>250 \text{ J/mm}^3$ ) the amount of Mn decreases. The formation of ferrite as primary phase is thus promoted and the amount of bcc- $\delta$  phase increases significantly in the final microstructure (Figure A7-d in Appendix A) [56,63–66]. Because of that, the fabrication of graded-microstructure samples using alloy A2 was possible through controlled evaporation of Mn. Since changes in the volatile element Mn content have a pronounced impact on the phase fractions in the samples (bcc- $\delta$  and fcc- $\gamma$ ), and the amount of evaporated Mn varies with the VED, the generally undesired selective evaporation of certain elements can be deliberately exploited to manipulate the phase composition in the final microstructure. A bcc- $\delta$ /fcc- $\gamma$  duplex microstructure with tailored amounts of the two phases can be fabricated simply by modifying the applied VED on a local scale. Following this approach, the example in Fig. 4 demonstrates the feasibility of microstructure tailoring during LPBF of SMAs via site-specific in-situ alloying. The very low speed of 100 mm/s was applied to evaporate a high amount of Mn and thus decrease the fcc- $\gamma$  stability and promote the formation of almost fully ferritic areas. As ferrite forms as the primary phase, it develops a  $\langle 001 \rangle$  texture along the BD (Fig. A8). The loss in Mn in the high-speed scanned regions is not so pronounced to induce a change in the primary solidification phase to ferrite (Fig. 4). The alloy solidifies primarily as austenite phase, as predicted from the empirical formulation for  $\text{Cr}_{\text{eq}}$  and  $\text{Ni}_{\text{eq}}$ , and a fully austenitic microstructure forms at these locations (Fig. A8) [39,67].

#### 4.2. Effect of rescanning on microstructure formation

Several factors explain the generation of an almost fully ferritic highly textured microstructure with rescanning, especially for the alloy A1 (Fig. 2). In the first place, the amount of Mn evaporation is particularly enhanced by the multiple rescanning of the same area [19], especially when low scanning speeds are used. Mn evaporation is induced during both the first and second scans (Fig. 10). Considering the role of Mn as an austenite stabilizer, its pronounced evaporation stabilizes the ferrite phase, preventing the formation of austenite in the final microstructure. The second factor to be considered is the roughness and the thermal conductivity of the base material, which affect the energy input from the laser and the cooling rate [35,68,69]. During the first

scan, the generated melt pools are in contact with a layer of powder (Fig. 10). During rescanning, the formed melt pools are entirely surrounded by solidified material (Fig. 10). The heat transfer conditions are therefore different for the first scan and the rescanning. Since the dense material has a higher heat-conductivity than the powder, heat is quickly dissipated from the melt pool into the surrounding dense material during the rescanning, resulting in a higher cooling rate.

The energy input from the laser into the material, which is finally converted into heat, also depends on the absorptivity of the material [69–72]. Tolochko et al. reported that the laser absorptivity of powders is approximately double that of dense material [73]. A reduced energy transfer is thus expected during rescanning, leading to the formation of shallower and narrower melt pools. The reduced energy input further contributes to an increase in the cooling rate within the melt pools generated with rescanning. This results in the (partial) suppression of the transformation bcc- $\delta \rightarrow$  fcc- $\gamma$  and the bcc- $\delta$  phase passes rapidly through the austenite phase field without transforming. This phenomenon can be visualized as if the bcc- $\delta$  ferrite by-passes the fcc- $\gamma$  phase [54,74–77]. The solidification in the melt pools generated during rescanning occurs similarly to the first-scan melt pools. However, the solidification of ferrite as the primary phase is even more favored because of the further decrease in Mn content, and its transformation to austenite during cooling is less probable due to the high cooling rate achieved.

From the EBSD images shown in Fig. 2, it is clear that rescanning increases the epitaxial growth through the sample during solidification, enhancing the texture of the ferrite phase along the BD [78]. The shallower melt pool generated with the second scan preferentially remelts the material near the top of the pool. Remelting does not eliminate the bcc- $\delta$  grain boundaries (GBs) in the bottom layers, but causes an extension of the ferrite GBs [79]. As the melt pool solidifies, grains exhibit epitaxial growth, aligning themselves with the orientation of the existing grains [55]. This process leads to the formation of columnar grains that can extend over multiple powder layers, reaching lengths of several hundred micrometers. Moreover, a highly noticeable  $\langle 001 \rangle$  texture is developed along the BD. The elongation of grains along the BD occurs as they grow in response to the vertical thermal gradient between the melt pool and the solidified layers at the bottom [54]. The formation of a  $\langle 001 \rangle$  texture is also promoted by the change in melt pool morphology in the second scan. Columnar grains grow with the easy growth directions  $\langle 001 \rangle$  closely aligned to the normal of the melt pool boundary [37]. Since the bottom of the shallower melt pools generated with the rescanning is nearly horizontally oriented, grains show a preferential alignment of the  $\langle 001 \rangle$  directions with the BD.

In the fabrication of graded-microstructure samples using the alloy A1, it can be seen that the use of a speed of 400 mm/s for the first scan seems to be ideal for producing an almost entirely austenitic microstructure through the bcc- $\delta \rightarrow$  fcc- $\gamma$  phase transformation, avoiding excessive Mn evaporation and rescanning-induced defects (Fig. 5-b). The reduction of the scanning speed to 250 mm/s or 300 mm/s for the second scan causes Mn evaporation and stabilizes the ferritic phase at the desired rescanned regions (scan velocity of 400 mm/s seems too high for this scope). In this way, important modifications in the microstructure can be introduced simply by local rescanning specific regions of the samples.

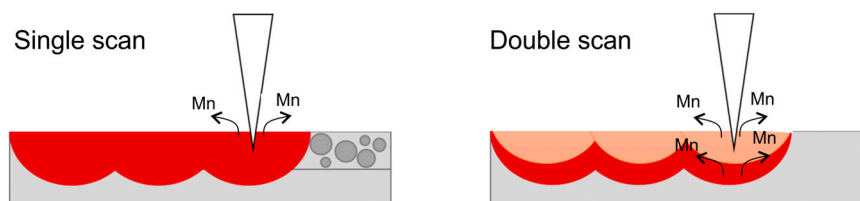


Fig. 10. Sketch detailing the melt pool formation and Mn evaporation during single and double (rescanning) scans.



The formation of austenite with the first scan is favored by the use of higher speed in the alloy A2 (Fig. 6). With a scanning speed of 600 mm/s a fully-austenitic microstructure with rather coarse grains is observed. This austenite phase is primary austenite that forms upon solidification. Indeed, austenite shows elongated grains along the BD with a preferential  $\langle 001 \rangle$  texture. As for alloy A1, low scanning speeds have to be applied to exploit the possibility of site-specific in-situ alloying offered by LPBF and form ferritic regions in the microstructure of the components. The use of rescanning in specific regions of the samples locally modifies the microstructure. The second scan at 250 mm/s favors the formation of ferrite through the reduction in Mn content caused by the multiple rescanning and the use of a rather slow speed in the second scan [63]. A high amount of fine austenite is still observed in the rescanned regions presumably due to the fact that part of the primary ferrite transforms to austenite upon cooling. Unlike alloy A1, the transformation from ferrite to austenite seems to be promoted in alloy A2 despite rescanning. The reduced Mn evaporation during scanning at 600 mm/s and the presence of C, which are both austenite stabilizers, leads to more austenite phase in the A2 samples with similar rescanning conditions.

For the layered sample of Fig. 6, it seems that higher amounts of ferrite form at the edges of the rescanned regions. At these locations, defined as laser-turn regions, the laser ends the line scan, turns direction, and starts with the subsequent line scan. The continuous back-and-forth movement of the laser during LPBF causes heat accumulation at these turn locations. As the melt pool formed at this region during the scanning of the previous track may not fully solidify while the subsequent track is being scanned, melt pool size and morphology are affected [67]. Melt pools often overlap and are bigger in size at these locations due to the residual heat from the previous track. For this reason, a more pronounced Mn evaporation and, subsequently, higher ferrite content have been observed at the borders of the rescanned regions. According to the numerical analysis reported in the work of Shrestha et al. [67], the magnitude of heat accumulation and melt pool overlap is generally higher for short scan lengths. Therefore, the highest amount of ferrite is observed in the R-0.25 mm sample, where the scan length of the rescanned region is 0.25 mm. Pronounced heat accumulation in this sample is also expected considering the fact the rescanned regions, which experience a significantly high heat input, are narrowly spaced.

These examples show how the tuning of the LPBF processing parameters can be applied for microstructure manipulation of SMA parts. This can be achieved by exploiting the fact that modifications in the alloys' composition can be introduced during LPBF and the applied processing parameters have a direct impact on the thermal history experienced by the material, affecting the solidification behavior and the phase transformation sequences in the processed alloys. In this way, site-specific modification in grain size, morphology and orientation, and phase volume fractions (fcc- $\gamma$  and bcc- $\delta$ ) can be induced, and different microstructures can be incorporated into a single component. These graded microstructure can significantly alter the mechanical and functional properties of the material. In the recent reports it is shown that a strength and ductility synergy is obtained in various engineering materials (e.g. pure Cu or Ti [80,81]) by promoting the formation of hybrid microstructures. In this context it is important to examine the mechanical and shape memory properties of the SMAs investigated in the present study.

#### 4.3. Effect of graded-microstructure on shape memory and mechanical properties

The possibility of generating graded microstructure allows for the fabrication of components with tunable properties. Significant variations in the mechanical and shape memory performance of the samples are observed due to changes in the scan speed or the use of rescanning. In the previous studies [3,25], improved strength and hardness were observed in those samples characterized by phase fractions of bcc- $\delta$

higher than 10% and relatively fine microstructure [3]. The ferrite phase is generally harder than the austenite and GBs act as obstacles for dislocation movements [82–84]. The increase in strength is achieved at the expense of the shape memory properties due to the fact that the ferrite phase is not involved in the martensitic transformation responsible for the SME [85,86]. A fully austenitic microstructure appears to be more appropriate to improve the shape memory performance with, however, a certain loss in strength. The idea of fabricating mixed-microstructure components aims to overcome this trade-off in the properties of Fe-SMAs fabricated by LPBF and manufacture samples with high strength without compromising the shape memory effect. The strength and shape memory properties of the mixed-microstructure sample fabricated by alternating different VEDs with alloy A2 (Fig. 7) lay in the middle of the two extreme cases of the single-scanned samples (100 mm/s and 400 mm/s samples). This means that the scanning of some regions of the sample at lower scanning speeds allows for increasing the strength of the sample without significantly reducing the shape memory properties (Fig. 7-c). The formation of bcc- $\delta$  ferrite significantly improves the material's hardness and strength in the locations scanned at the lowest speed of 100 mm/s (Fig. 7-d). Based on these results, it is evident that the stacking sequence of areas with different microstructures has an influence on the mechanical properties of the LPBF-fabricated SMAs. The strength-SME trade-off can be partially overcome. The reported examples can be seen as a proof of concept of the possibility of local microstructure manipulation during LPBF and its advantages. The local and full control of the microstructure and its effects on the material's functionalities are demonstrated. Further potential is seen if this possibility of microstructure control is exploited to modify extent and distribution of the different-microstructure areas based on the desired properties. For example, regions scanned at low speeds could be extended when higher strength is required. These areas should be confined to applications where the SME rather than the strength is important. Using this strategy of microstructure manipulation, parts that show SME or high strength only in specific locations could also be fabricated.

Rescanning also increases the strength of the alloy A2 due to grain refinement and formation of ferrite phase in the microstructure. The formation of ferrite, however, deteriorates the SME of the material. As the ferrite phase does not contribute to the alloy's SME, the recovery strain decreases from 0.63% for the NO-R sample to 0.49% for the R-0.25 mm sample. It can be assumed that because of the reduced amount of ferrite in the NO-R sample a relatively high amount of martensite forms during pre-straining. Its back transformation to fcc- $\gamma$  causes considerable shape recovery during heating. The increase in the ferrite phase with the rescanning reduces the amount of hcp- $\epsilon$  that can form via the fcc- $\gamma \rightarrow$  hcp- $\epsilon$  transformation during loading and transform back during heating, causing an overall decrease in the SME. Some shape memory effect is activated, but it is not enough to prevent the effect of thermal expansion. The reduction in the SME is not very pronounced for the other two rescanned samples, especially for the sample R-1 mm, for which a recovery strain of 0.6% is measured at 200 °C. Considering that for this sample, the stress at 2% increases by more than 40 MPa compared to the single-scanned sample, it can be stated that appropriate use of rescanning can be applied to improve the strength of the material without compromising the shape memory properties. The very high strength achieved for the rescanned samples might also result from the so-called Bauschinger effect, which is observed with multiphase materials or materials with heterogeneous structures that have different strengths and deformation abilities [87]. The difference in plastic deformation of different areas causes constraints and back stress in the softer regions making them appear stronger (hetero-deformation induced strengthening [88]). The global strength of the component is in this way improved [89]. In order to confirm this, further investigations are required, involving microstructure investigation on a microscale and in-situ deformation monitoring [90].

In addition to the lower strength due to the coarser grains and less

ferrite content in the microstructure, the reduced yield stress of the NO-R sample can be linked to the easy and more pronounced martensite formation, which is expected to occur during the loading of this sample containing the highest amount of transformable austenite. The onset of the deformation-induced martensitic transformation causes an early and more pronounced non-linearity in the stress-strain curve [40]. With the activation of the SME under constraints, the  $\sigma_{\text{rec}}$  developed during the cooling stage can be sufficiently high to induce again the transformation  $\text{fcc-}\gamma \rightarrow \text{hcp-}\epsilon$  and exceed the yield strength of the material, causing a certain bending in the curve recovery stress versus temperature [2,4]. This explains why all the investigated samples show comparable final recovery stress at RT despite the different SME. Because of its lower strength (lowest yield strength among all the samples) and more pronounced martensite transformation (highest amount of austenite in the as-fabricated condition), during cooling the single-scanned sample experiences an early bending of the recovery stress-temperature curve (Fig. 8-f). Therefore, despite the higher  $\sigma_{\text{rec}}$  value measured at 200 °C, the final  $\sigma_{\text{rec}}$  value is the same or even lower than for the rescanned samples. This indicates that increasing the SME does not necessary lead to higher recovery stress [4]. The opposite effect is observed for the sample R-0.25 mm, which shows the lowest  $\sigma_{\text{rec}}$  at 200 °C but the highest value at RT. Because of the finer microstructure and the larger amount of ferrite introduced during rescanning, the movement of perfect dislocations and the phase transformation to  $\text{hcp-}\epsilon$  martensite are confined, increasing the yield strength of the sample. The highest yield strength results in a recovery stress-temperature curve that increases almost linearly during cooling, reaching extremely high recovery stress values at RT (494 MPa). The lowest  $\sigma_{\text{rec}}$  values are achieved for the samples R-1 mm and R-0.5 mm, for which neither the SME nor the yield strength are particularly high. The recovery stress associated to the SME is lower at RT compared to the single-scanned sample and the curve bending during cooling is more pronounced and occurs at lower stress compared to the R-0.25 mm sample.

PE is defined by the amount of the  $\text{fcc-}\gamma \leftrightarrow \text{hcp-}\epsilon$  transformation, and the formation and (forward-back) movement of stacking faults (SFs) in the austenitic matrix. The martensitic transformation and the formation/movement of SFs are facilitated by a high amount of transformable austenite in the material prior to deformation, fine-grained microstructure and high strength of the material [4,91]. The NO-R sample is mainly characterized by an austenitic microstructure. Compared to the rescanned samples, however, the austenite grains are rather coarse and the strength of the sample is lower. This leads to a PE that is rather pronounced ( $\epsilon_{\text{pse}}$  of  $0.415 \pm 0.006\%$ ) but lower than the  $\epsilon_{\text{pse}}$  of the R-1 mm and R-0.5 mm samples. For the latter, the combination of fine-grained microstructure, high strength, and relatively low amount of ferrite leads to  $\epsilon_{\text{pse}}$  of  $0.435 \pm 0.004\%$  and  $0.428 \pm 0.004\%$ , respectively. Despite the highest strength and the finest microstructure of the R-0.25 mm sample,  $\epsilon_{\text{pse}}$  reduces compared to the previous cases due to the increased amount of ferrite, which rises to almost 30%.

As for the previous case of the samples fabricated using different scanning speeds, the location and extent of rescanning can be easily adjusted, giving the possibility of tuning the mechanical and shape memory properties. Larger areas of the sample can be rescanned when high strength rather than shape recovery is required. Contrary, rescanning can be applied in limited and narrower areas of the sample to achieve good shape recovery in combination with some increase in strength.

It is worth noting that, despite the presence of a few lack of fusion defects and keyhole pores, a very good performance of the samples fabricated with different speeds at different locations as well as with rescanning is achieved in. All samples could be pre-strained up to 2% without problems of fracturing, and a very high strength has been measured. The orientation of the lack of fusion defects with respect to the LD probably plays a crucial role. These defects are indeed oriented parallel to the LD of the samples. Generally when oriented perpendicular to the LD they have a much more detrimental effect, causing high stress

concentration at their edges [92,93].

This study provides effective and innovative strategies for microstructure manipulation during LPBF of SMAs, highlighting the great potential of this process for the development of materials with enhanced performance, customized properties, and improved functionality. The findings extend beyond the specific alloys investigated and have broad implications for the fabrication of other alloys containing volatile elements. This opens up possibilities for the development of tailored materials with unique properties and performance.

## 5. Conclusions

This work shows the feasibility of site-specific control of the microstructure of the Fe-17Mn-5Si-10Cr-4Ni and Fe-17Mn-5Si-10Cr-4Ni-(VC) SMAs. Components with tailored phase volume fractions, grain size, and orientation are fabricated by varying the processing parameters. In particular, different microstructures can be integrated within single components when the scanning velocity or the scanning strategy are locally tuned. Based on the obtained results, several conclusions can be drawn:

1. The Fe-17Mn-5Si-10Cr-4Ni SMA solidifies as bcc- $\delta$  ferrite when high scan velocities are applied. The use of lower scanning speeds promotes the transformation of the primary bcc- $\delta$  ferrite to  $\text{fcc-}\gamma$  austenite during cooling, leading to the formation of a fine fully austenitic microstructure.
2. A different solidification behavior is observed for the Fe-17Mn-5Si-10Cr-4Ni-(VC) SMA, whose primary phase is  $\text{fcc-}\gamma$  austenite when processed with high scanning speeds. The addition of C (austenite stabilizer) increases the stability of austenite. Some ferrite formation and austenite grain refinement are introduced by using low scanning speeds. The austenite stability decreases with the evaporation of the austenite stabilizer Mn induced during the process.
3. The use of rescanning also promotes the formation of ferrite through pronounced Mn evaporation. Higher cooling rate are also achieved in the melt pools during the second scanning, thus limiting the  $\text{bcc-}\delta \rightarrow \text{fcc-}\gamma$  transformation during cooling.
4. The variations in the phase volume fraction and grain size/orientation induced by changing the scan velocity or using the rescanning strategy can be exploited to locally modify the microstructure of LPBF components and build graded-microstructure samples. Local variations in grain size and orientation, and in phase fractions and distribution are induced in specific areas of the LPBF-fabricated samples by controlling the thermal history and the amount of Mn in the material. Such parts with hybrid microstructure can only be fabricated by LPBF.
5. Following this approach, SMA samples with unique thermo-mechanical properties can be fabricated. An excellent combination of pronounced shape memory properties and ultrahigh strength can be achieved.

This research highlights the potential of additive manufacturing for the production of advanced alloys, paving the way for the development of innovative and high-performance materials with tailored microstructures and properties.

## CRedit authorship contribution statement

**Irene Ferretto:** Conceptualization, Methodology, Validation, Investigation, Data curation, Visualization, Writing – original draft. **Amit Sharma:** Methodology, Validation, Investigation, Data curation, Writing – review & editing. **Dohyung Kim:** Validation, Investigation. **Nicolo' Maria della Ventura:** Validation, Investigation, Review & editing. **Xavier Maeder:** Validation, Investigation, Review & editing. **Johann Michler:** Review & editing. **Ehsan Hosseini:** Validation, Investigation, Writing – review & editing. **Wookjin Lee:**

Conceptualization, Review & editing, Funding acquisition, Supervision.  
**Christian Leinenbach:** Conceptualization, Writing – review & editing, Funding acquisition, Project administration, Supervision.

#### Declaration of Competing Interest

The authors declare that they have no known competing financial interests or personal relationships that could have appeared to influence the work reported in this paper.

#### Data availability statement

The data presented in this work will be made available upon

reasonable request.

#### Acknowledgements

The work is funded by the Swiss National Science Foundation (SNSF) through the project IZKSZ2\_188290/1 and the National Research Foundation of Korea (NRF) under the grant number 2019K1A3A1A14065695, which is gratefully acknowledged. The authors thank voestalpine BÖHLER Edelstahl GmbH & Co KG for providing the alloy powder A2.

#### Appendix A

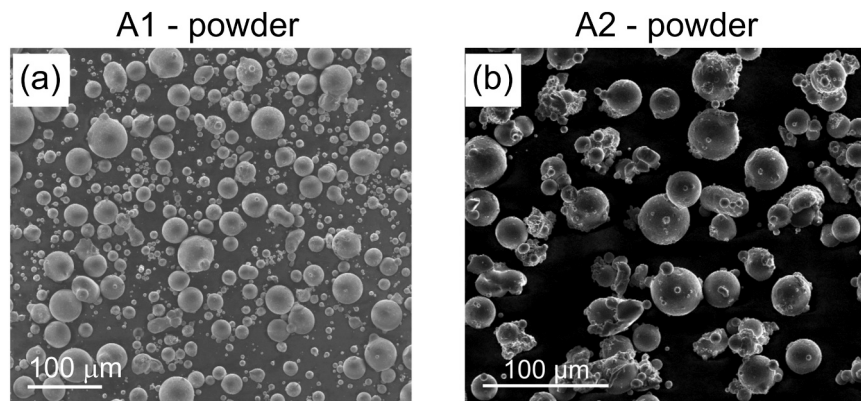


**Fig. A1.** SEM images of the two powders, alloy 1-A1 (a), and alloy 2-A2 (b).

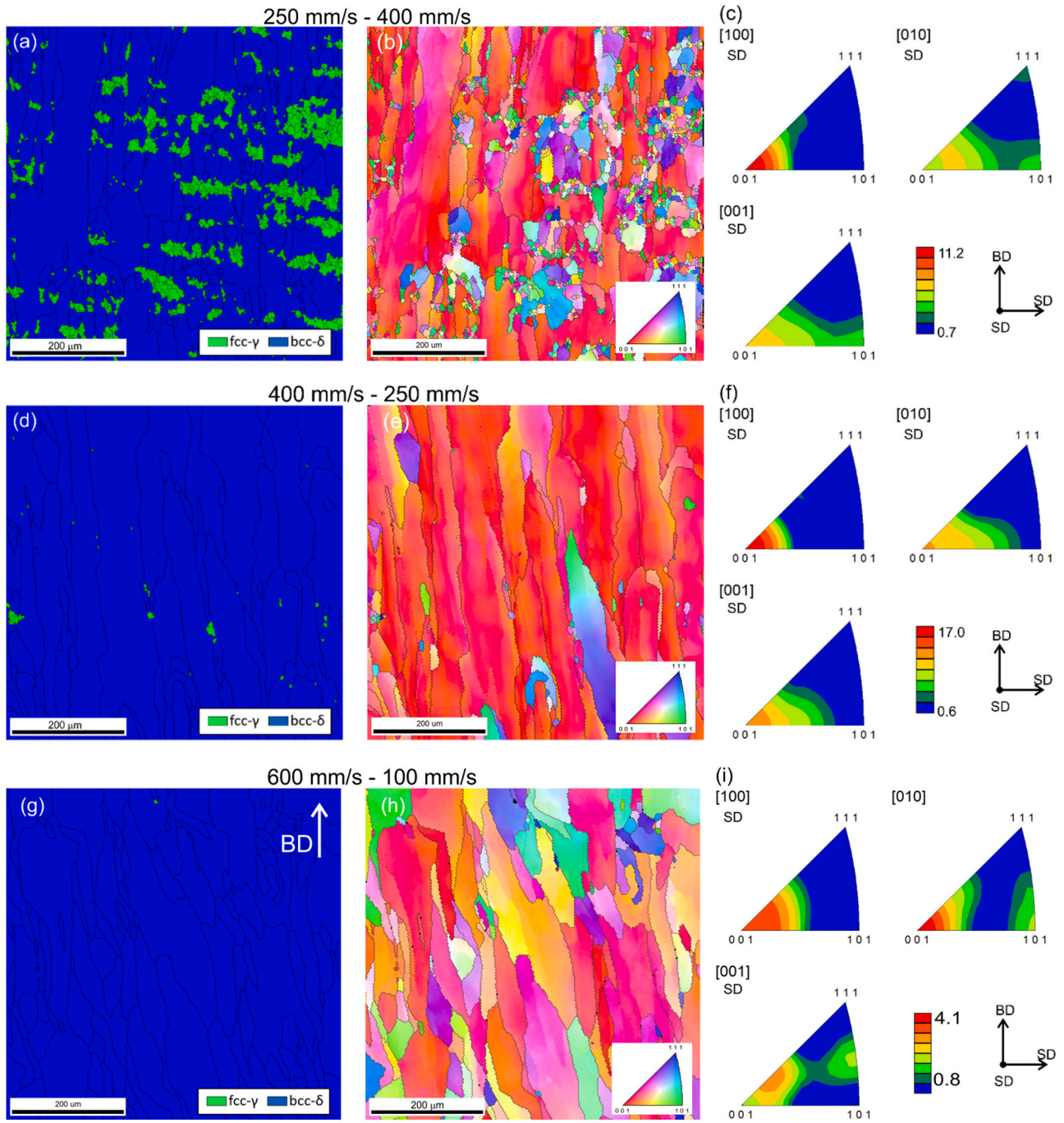


**Fig. A2.** EBSD maps with phase coloring (a,d,g), EBSD maps with IPF coloring related to the BD (b,e,h) and IPFs related to the BD and the two SDs (c,f,i) of the samples fabricated using rescanning (scanning speeds of the first and second scans are reported on the top of the images).



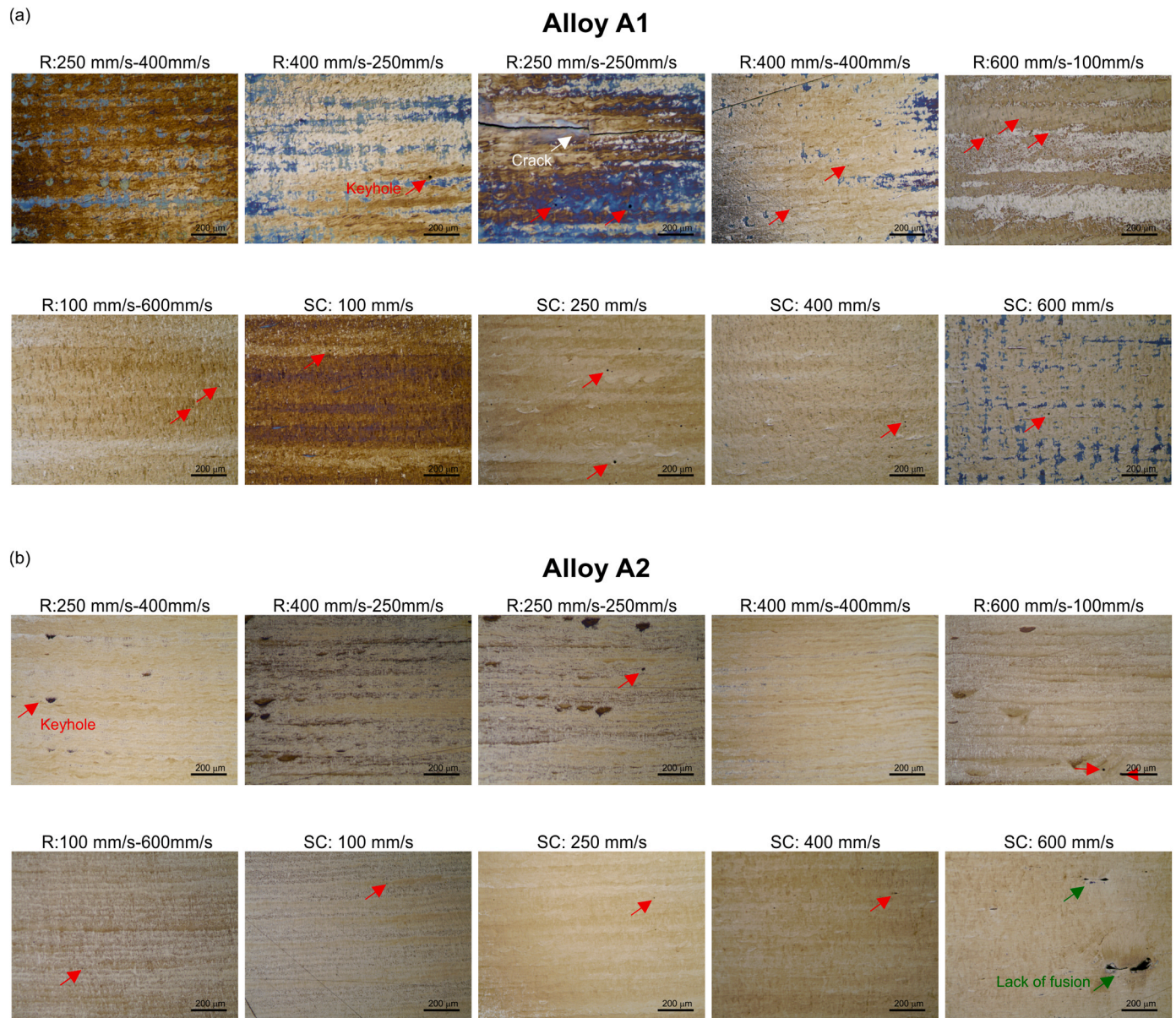


**Fig. A3.** OM of the samples fabricated at different scanning speeds (single scan, SC) and with different rescanning conditions (rescanning, R) from the alloy A1 (a) and A2 (b), showing the formation of a few defects; the contrast in the pictures is caused by etching originally performed to identify the different phases.

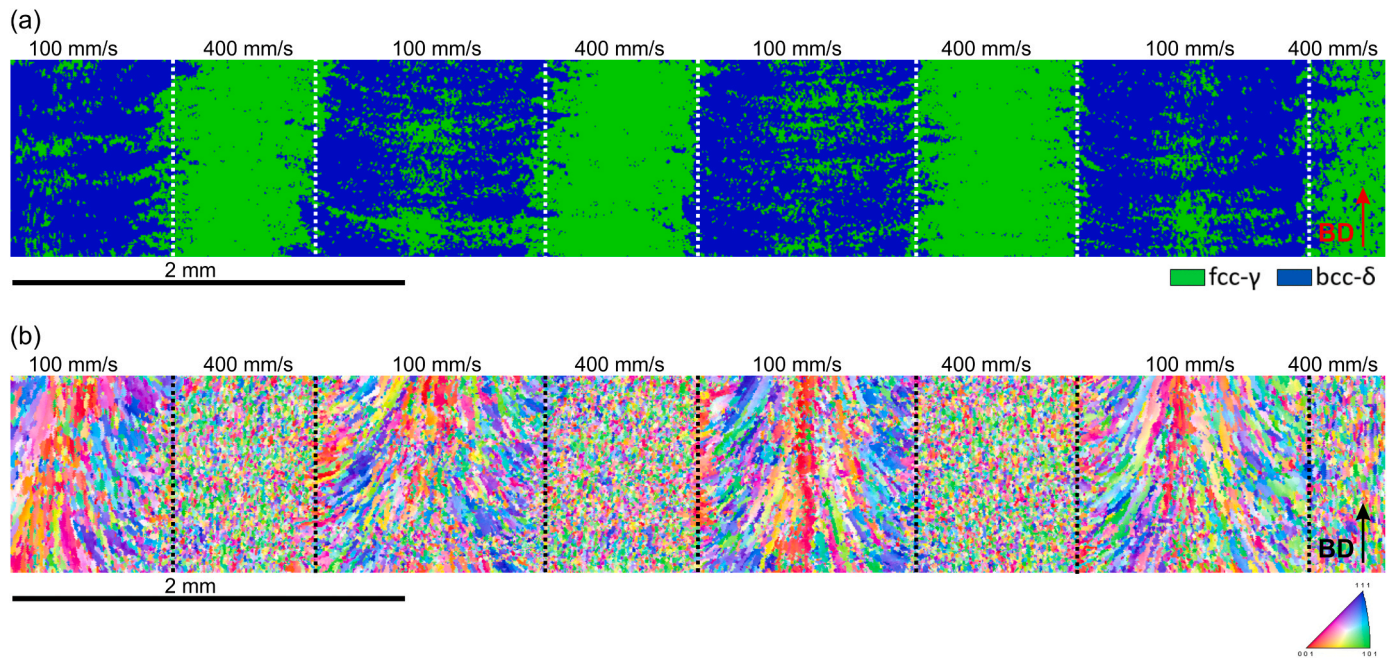


**Fig. A4.** EBSD analysis of the sample fabricated using alternation of different scanning speeds, 400 mm/s and 100 mm/s; EBSD maps with phase (a) and IPF coloring (b) of the sample.



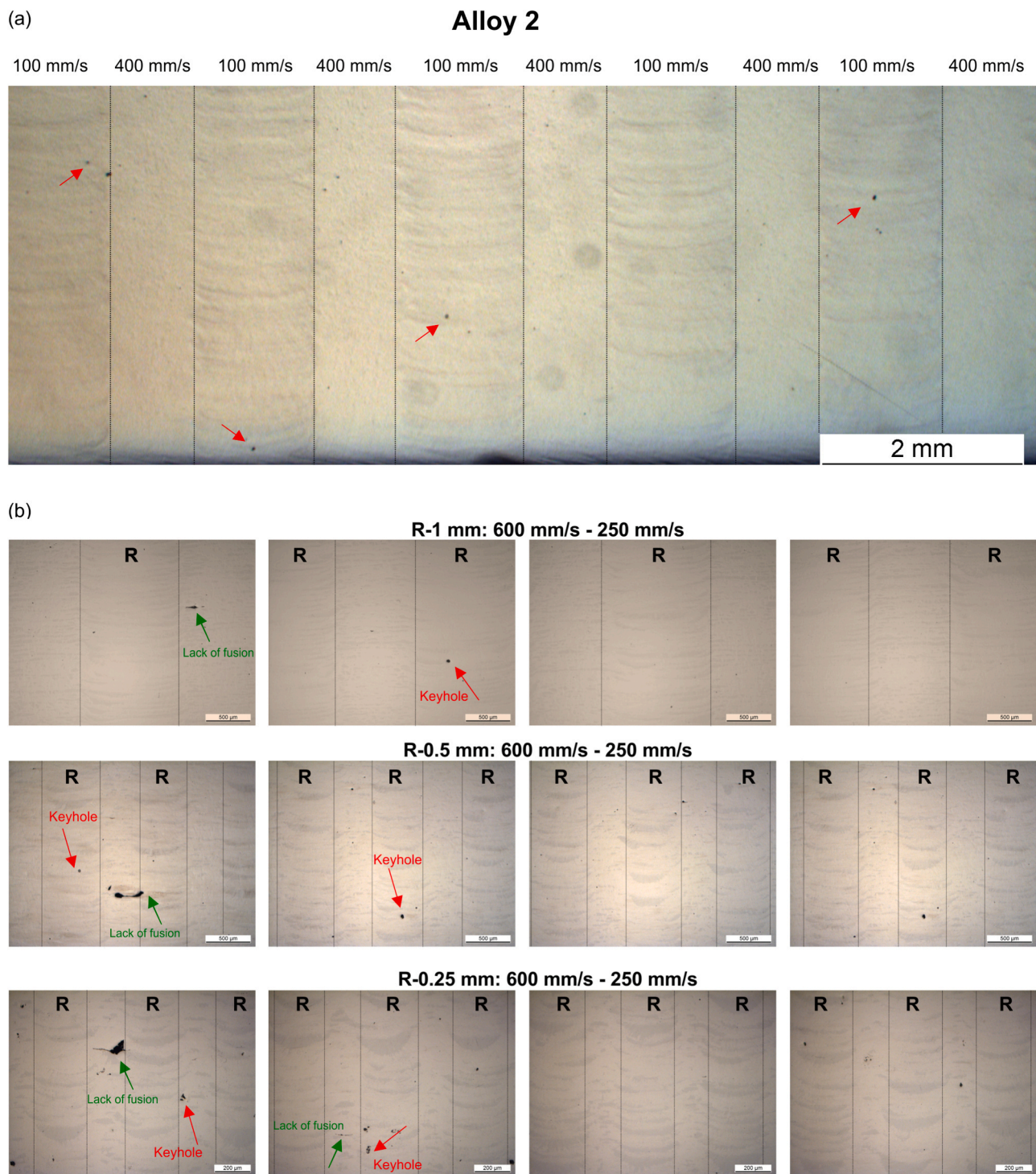


**Fig. A5.** OM of the sample fabricated by alternating different scanning speeds, 400 mm/s and 100 mm/s (Alloy 2) (a); OM of the samples fabricated by rescanning, 600 mm/s and 250 mm/s (Alloy 2) (b).

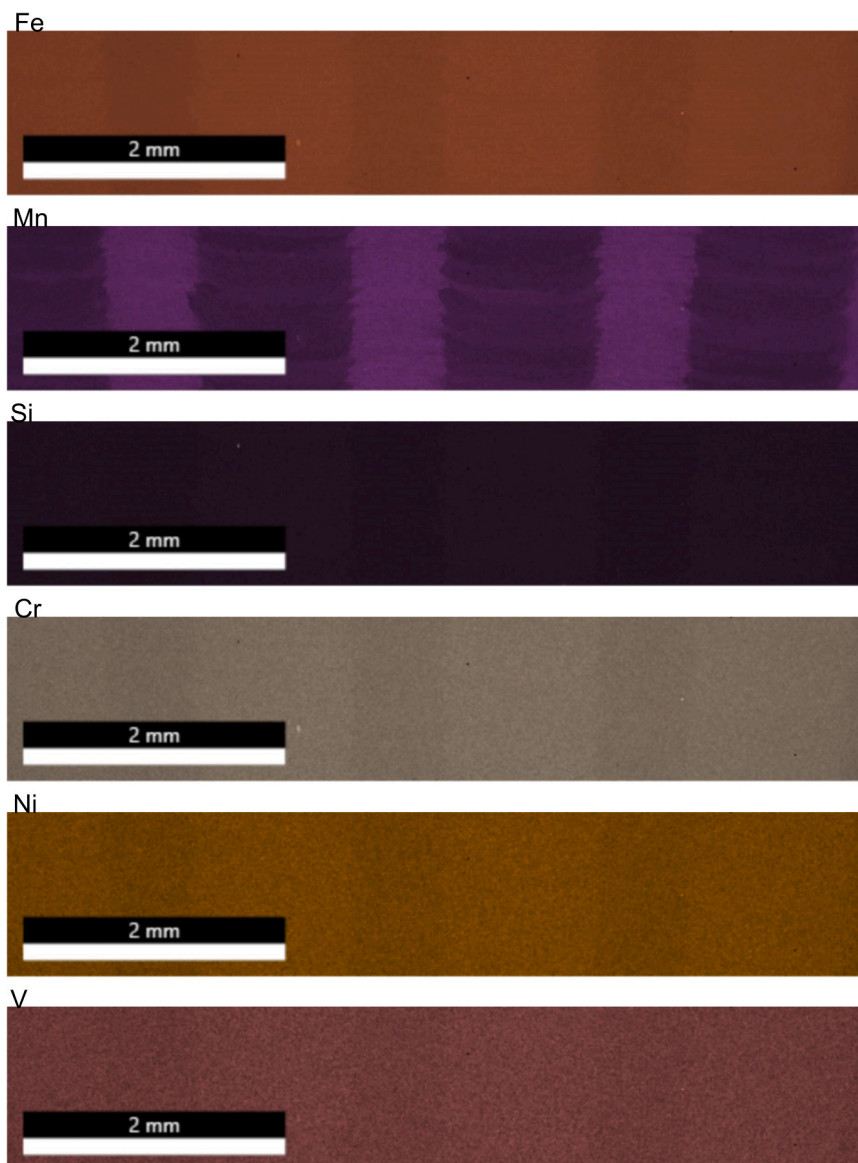


**Fig. A6.** EDS maps of the sample fabricated using alternation of different speeds (600 mm/s and 100 mm/s), showing the distribution of Fe, Mn, Si, Cr, Ni and V within the sample.



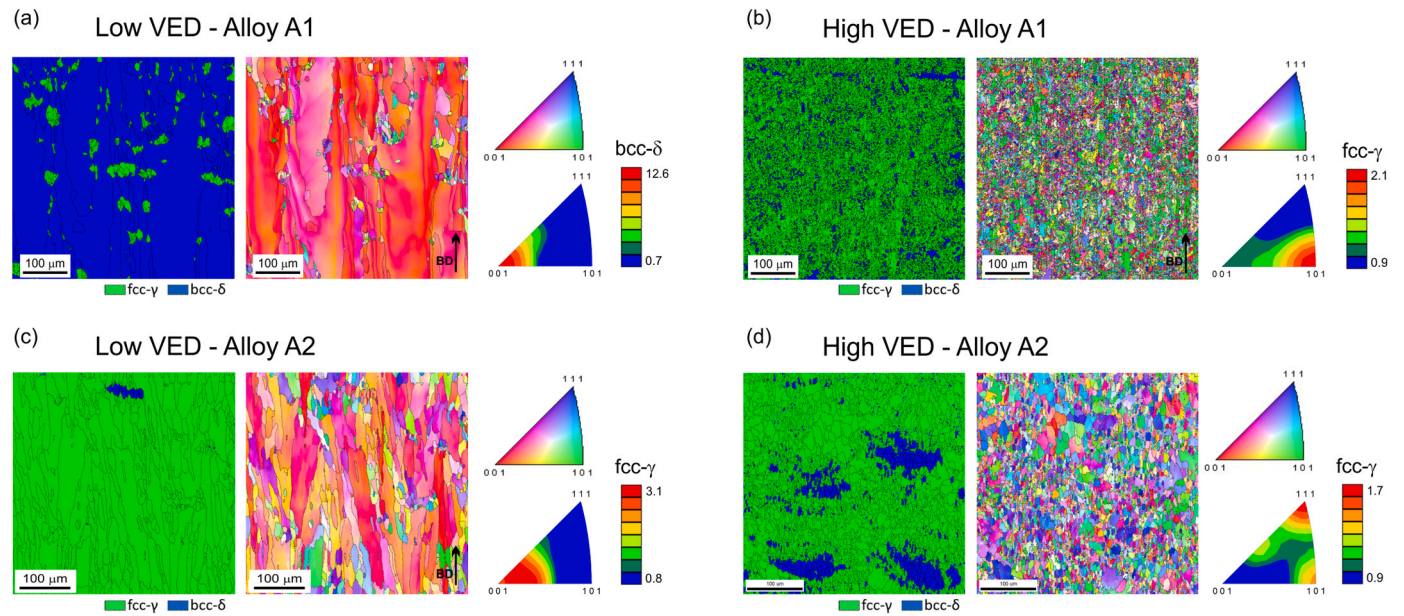


**Fig. A7.** EBSD maps with phase coloring and IPF coloring, and IPFs for the alloy A1 fabricated at low VED (a) and high VED (b); EBSD maps with phase coloring and IPF coloring, and IPFs for the alloy A2 fabricated at low VED (c) and high VED (d).

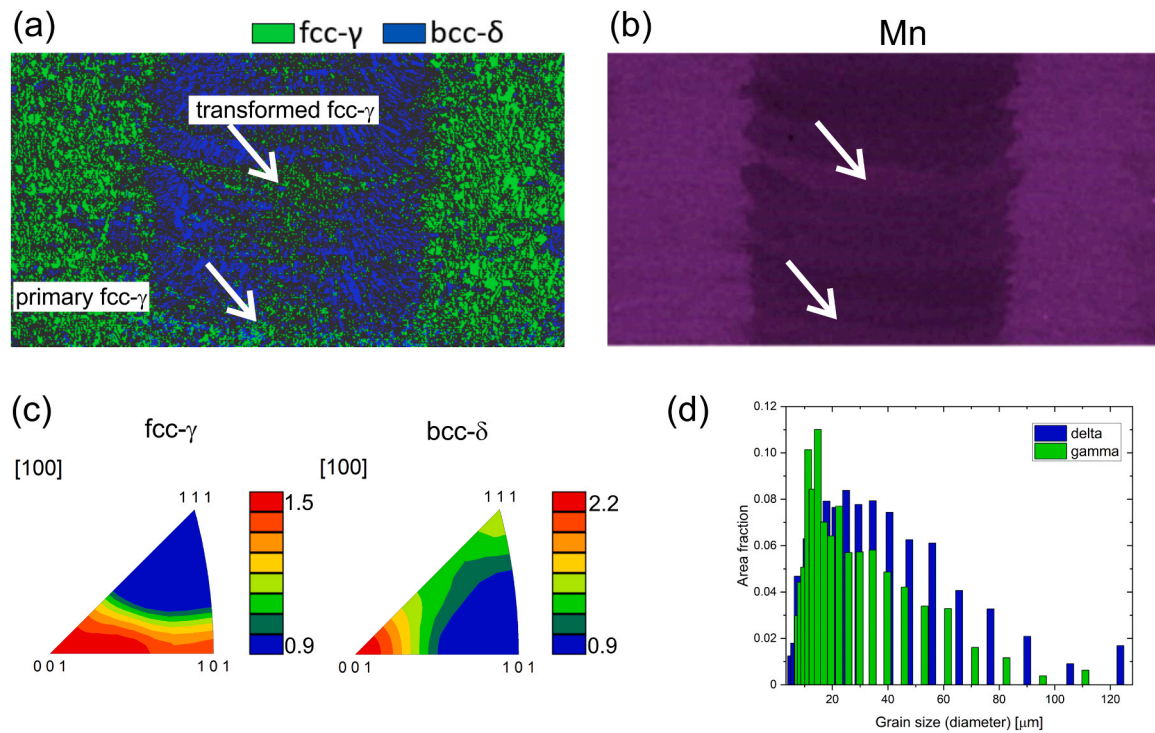


**Fig. A8.** EBSD maps with phase coloring (a) and EDS map showing Mn distribution (b); IPFs and grain size distribution (d) of the fcc-γ phase and bcc-δ phase related to the BD of the sample fabricated using alternation of two different scanning speeds (600 mm/s and 100 mm/s).

**Table A 1**

List of samples fabricated using rescanning; scanning speeds applied for the first and second scans are reported.

Alloy	Sample	First scan speed (mm/s)	Second scan speed (mm/s)
A1	R-250/400	250	400
A1	R-400/250	400	250
A1	R-250/250	250	250
A1	R-400/400	400	400
A1	R-600/100	600	100
A1	R-100/600	100	600
A2	R-250/400	250	400

(continued on next page)

Table A 1 (continued)

Alloy	Sample	First scan speed (mm/s)	Second scan speed (mm/s)
A2	R-400/250	400	250
A2	R-250/250	250	250
A2	R-400/400	400	400
A2	R-600/100	600	100
A2	R-100/600	100	600

## References

- [1] A. Cladera, B. Weber, C. Leinenbach, C. Czaderski, M. Shahverdi, M. Motavalli, Iron-based shape memory alloys for civil engineering structures: an overview, *Constr. Build. Mater.* 63 (2014) 281–293, <https://doi.org/10.1016/j.conbuildmat.2014.04.032>.
- [2] Y. Yang, A. Arabi-Hashemi, C. Leinenbach, M. Shahverdi, Influence of thermal treatment conditions on recovery stress formation in an FeMnSi-SMA, *Mater. Sci. Eng.: A* 802 (2021), 140694, <https://doi.org/10.1016/j.msea.2020.140694>.
- [3] I. Ferretto, A. Borzi, D. Kim, N.M.D. Ventura, E. Hosseini, W.J. Lee, C. Leinenbach, Control of microstructure and shape memory properties of a Fe-Mn-Si-based shape memory alloy during laser powder bed fusion, *Addit. Manuf. Lett.* 3 (2022), 100091, <https://doi.org/10.1016/j.addlet.2022.100091>.
- [4] A. Arabi-Hashemi, W.J. Lee, C. Leinenbach, Recovery stress formation in FeMnSi based shape memory alloys: impact of precipitates, texture and grain size, *Mater. Des.* 139 (2018) 258–268, <https://doi.org/10.1016/j.matdes.2017.11.006>.
- [5] I. Ferretto, D. Kim, N.M. Della Ventura, M. Shahverdi, W. Lee, C. Leinenbach, Laser powder bed fusion of a Fe-Mn-Si shape memory alloy, *Addit. Manuf.* 46 (2021), 102071, <https://doi.org/10.1016/j.addma.2021.102071>.
- [6] O. Matsumura, S. Furusako, T. Furukawa, H. Otsuka, Formation of Surface Texture and Anisotropy of Shape Memory Effect in an Fe-Mn-Si Alloy, *ISIJ Int.* 36 (1996) 1103–1108, <https://doi.org/10.2355/isijinternational.36.1103>.
- [7] M.-S. Pham, B. Dovsky, P.A. Hooper, C.M. Gourlay, A. Piglion, The role of side-branching in microstructure development in laser powder-bed fusion, *Nat. Commun.* 11 (2020) 749, <https://doi.org/10.1038/s41467-020-14453-3>.
- [8] M. Higashi, T. Ozaki, Selective laser melting of pure molybdenum: evolution of defect and crystallographic texture with process parameters, *Mater. Des.* 191 (2020), 108588, <https://doi.org/10.1016/j.matdes.2020.108588>.
- [9] V.A. Popovich, E.V. Borisov, A.A. Popovich, V.Sh. Sufiurov, D.V. Masaylo, L. Alzina, Functionally graded Inconel 718 processed by additive manufacturing: crystallographic texture, anisotropy of microstructure and mechanical properties, *Mater. Des.* 114 (2017) 441–449, <https://doi.org/10.1016/j.matdes.2016.10.075>.
- [10] R.R. Dehoff, M.M. Kirka, W.J. Sames, H. Bilheux, A.S. Tremsin, L.E. Lowe, S. Babu, Site specific control of crystallographic grain orientation through electron beam additive manufacturing, *Mater. Sci. Technol.* 31 (2015) 931–938, <https://doi.org/10.1179/1743284714Y.00000000734>.
- [11] F. Geiger, K. Kunze, T. Etter, Tailoring the texture of IN738LC processed by selective laser melting (SLM) by specific scanning strategies, *Mater. Sci. Eng.: A* 661 (2016) 240–246, <https://doi.org/10.1016/j.msea.2016.03.036>.
- [12] K.A. Sofinowski, S. Raman, X. Wang, B. Gasky, M. Seita, Layer-wise engineering of grain orientation (LEGO) in laser powder bed fusion of stainless steel 316L, *Addit. Manuf.* 38 (2021), 101809, <https://doi.org/10.1016/j.addma.2020.101809>.
- [13] B. Van der Schueren, J.P. Kruth, Powder deposition in selective metal powder sintering, *Rapid Prototyp. J.* 1 (1995) 23–31, <https://doi.org/10.1108/13552549510094241>.
- [14] H. Helmer, A. Bauereiß, R.F. Singer, C. Körner, Grain structure evolution in Inconel 718 during selective electron beam melting, *Mater. Sci. Eng.: A* 668 (2016) 180–187, <https://doi.org/10.1016/j.msea.2016.05.046>.
- [15] C. Sofras, J. Capek, A. Arabi-Hashemi, C. Leinenbach, M. Frost, K. An, R.E. Logé, M. Strobl, E. Polatidis, Tailored deformation behavior of 304L stainless steel through control of the crystallographic texture with laser-powder bed fusion, *Mater. Des.* 219 (2022), 110789, <https://doi.org/10.1016/j.matdes.2022.110789>.
- [16] N. Raghavan, S. Simunovic, R. Dehoff, A. Plotkowski, J. Turner, M. Kirka, S. Babu, Localized melt-scan strategy for site specific control of grain size and primary dendrite arm spacing in electron beam additive manufacturing, *Acta Mater.* 140 (2017) 375–387, <https://doi.org/10.1016/j.actamat.2017.08.038>.
- [17] Y.S. Lee, M.M. Kirka, R.B. Dinwiddie, N. Raghavan, J. Turner, R.R. Dehoff, S. Babu, Role of scan strategies on thermal gradient and solidification rate in electron beam powder bed fusion, *Addit. Manuf.* 22 (2018) 516–527, <https://doi.org/10.1016/j.addma.2018.04.038>.
- [18] S. Griffiths, M.D. Rossell, J. Croteau, N.Q. Vo, D.C. Dunand, C. Leinenbach, Effect of laser rescanning on the grain microstructure of a selective laser melted Al-Mg-Zr alloy, *Mater. Charact.* 143 (2018) 34–42, <https://doi.org/10.1016/j.matchar.2018.03.033>.
- [19] A. Arabi-Hashemi, X. Maeder, R. Figi, C. Schreiner, S. Griffiths, C. Leinenbach, 3D magnetic patterning in additive manufacturing via site-specific in-situ alloy modification, *Appl. Mater. Today* 18 (2020), 100512, <https://doi.org/10.1016/j.apmt.2019.100512>.
- [20] A.N. Alagha, S. Hussain, W. Zaki, Additive manufacturing of shape memory alloys: a review with emphasis on powder bed systems, *Mater. Des.* 204 (2021), 109654, <https://doi.org/10.1016/j.matdes.2021.109654>.
- [21] Z.X. Khoo, Y. Liu, J. An, C.K. Chua, Y.F. Shen, C.N. Kuo, A review of selective laser melted NiTi shape memory alloy, *Materials* 11 (2018) 519, <https://doi.org/10.3390/ma11040519>.
- [22] S. Dadbakhsh, M. Speirs, J.-P. Kruth, J. Schrooten, J. Luyten, J. Van Humbeeck, Effect of SLM parameters on transformation temperatures of shape memory nickel titanium parts, *Adv. Eng. Mater.* 16 (2014) 1140–1146, <https://doi.org/10.1002/adem.201300558>.
- [23] H. Meier, C. Haberland, J.F. R. Zarnetta, Selective laser melting of NiTi shape memory components, in: *Innovative Developments in Design and Manufacturing*, CRC Press, 2009.
- [24] T. Niendorf, F. Brenne, P. Krooß, M. Vollmer, J. Günther, D. Schwarze, H. Biermann, Microstructural evolution and functional properties of Fe-Mn-Al-Ni shape memory alloy processed by selective laser melting, *Met. Mater. Trans. A* 47 (2016) 2569–2573, <https://doi.org/10.1007/s11661-016-3412-z>.
- [25] X. Yang, L. Cheng, H. Peng, B. Qian, L. Yang, Y. Shi, A. Chen, Z. Zhang, L. Zhao, N. Hu, C. Yan, Y. Shi, Development of Fe-Mn-Si-Cr-Ni shape memory alloy with ultrahigh mechanical properties and large recovery strain by laser powder bed fusion, *J. Mater. Sci. Technol.* 150 (2023) 201–216, <https://doi.org/10.1016/j.jmst.2022.11.046>.
- [26] D. Kim, I. Ferretto, C. Leinenbach, W. Lee, W. Kim, Effect of direct aging on microstructure, mechanical properties and shape memory behavior of Fe-17Mn-5Si-10Cr-4Ni-(V, C) shape memory alloy fabricated by laser powder bed fusion, *Mater. Charact.* 197 (2023), 112705, <https://doi.org/10.1016/j.matchar.2023.112705>.
- [27] C. Czaderski, B. Weber, M. Shahverdi, M. Motavalli, C. Leinenbach, W. Lee, R. Brönnimann, J. Michels, Iron-based shape memory alloys (Fe-SMA) - a new material for prestressing concrete structures, *Proceedings of SMAR 2015 the 3rd Conference on Smart Monitoring, Assessment and Rehabilitation of Civil Structures*, (2015) (12 pp.).
- [28] M. Hauser, M. Wendler, A. Weiß, J. Mola, Quantification of deformation-induced  $\alpha'$ -martensite content in Fe-19Cr-3Mn-4Ni-0.15C-0.17N austenitic stainless steel by in-situ magnetic measurements, in: 2015.
- [29] C. Leinenbach, H. Kramer, C. Bernhard, D. Eifler, Thermo-mechanical properties of an Fe-Mn-Si-Cr-Ni-VC shape memory alloy with low transformation temperature, *Adv. Eng. Mater.* 14 (2012) 62–67, <https://doi.org/10.1002/adem.201100129>.
- [30] J. Lee, Y.C. Shin, Effects of composition and post heat treatment on shape memory characteristics and mechanical properties for laser direct deposited nitinol, *Lasers Manuf. Mater. Process.* 6 (2019) 41–58, <https://doi.org/10.1007/s40516-019-0079-5>.
- [31] Q. Ren, C. Chen, Z. Lu, X. Wang, H. Lu, S. Yin, Y. Liu, H. Li, J. Wang, Z. Ren, Effect of a constant laser energy density on the evolution of microstructure and mechanical properties of NiTi shape memory alloy fabricated by laser powder bed fusion, *Opt. Laser Technol.* 152 (2022), 108182, <https://doi.org/10.1016/j.optlastec.2022.108182>.
- [32] N.S. Moghaddam, S. Saedi, A. Amerinatanzi, A. Hinojos, A. Ramazani, J. Kundin, M.J. Mills, H. Karaca, M. Elahinia, Achieving superelasticity in additively manufactured NiTi in compression without post-process heat treatment, *Sci. Rep.* 9 (2019) 1–11.
- [33] M. Shahverdi, J. Michels, C. Czaderski, M. Motavalli, Iron-based shape memory alloy strips for strengthening RC members: material behavior and characterization, *Constr. Build. Mater.* 173 (2018) 586–599, <https://doi.org/10.1016/j.conbuildmat.2018.04.057>.
- [34] W.J. Lee, B. Weber, C. Leinenbach, Recovery stress formation in a restrained Fe-Mn-Si-based shape memory alloy used for prestressing or mechanical joining, *Constr. Build. Mater.* 95 (2015) 600–610, <https://doi.org/10.1016/j.conbuildmat.2015.07.098>.
- [35] C. Kneel, G. Dasargyri, T. Bauer, A. Colella, A.B. Spierings, C. Leinenbach, K. Wegener, Selective laser melting of an oxide dispersion strengthened (ODS)  $\gamma$ -TiAl alloy towards production of complex structures, *Mater. Des.* 134 (2017) 81–90, <https://doi.org/10.1016/j.matdes.2017.08.034>.
- [36] E. Yasa, J. Deckers, J. Kruth, The investigation of the influence of laser re-melting on density, surface quality and microstructure of selective laser melting parts, *Rapid Prototyp. J.* 17 (2011) 312–327, <https://doi.org/10.1108/13552541111156450>.
- [37] D. Herzog, V. Seyda, E. Wycisk, C. Emmelmann, Additive manufacturing of metals, *Acta Mater.* 117 (2016) 371–392, <https://doi.org/10.1016/j.actamat.2016.07.019>.
- [38] S. Cacace, G. Semeraro, On the Lack of fusion porosity in L-PBF processes, *Procedia CIRP* 112 (2022) 352–357, <https://doi.org/10.1016/j.procir.2022.09.008>.
- [39] T. DebRoy, H.L. Wei, J.S. Zuback, T. Mukherjee, J.W. Elmer, J.O. Milewski, A. M. Beese, A. Wilson-Heid, A. De, W. Zhang, Additive manufacturing of metallic components – Process, structure and properties, *Prog. Mater. Sci.* 92 (2018) 112–224, <https://doi.org/10.1016/j.pmatsci.2017.10.001>.



- [40] W.J. Lee, B. Weber, G. Feltrin, C. Czaderski, M. Motavalli, C. Leinenbach, Phase transformation behavior under uniaxial deformation of an Fe-Mn-Si-Cr-Ni-VC shape memory alloy, *Mater. Sci. Eng.: A* 581 (2013) 1–7, <https://doi.org/10.1016/j.msea.2013.06.002>.
- [41] C.-H. Yang, H.-C. Lin, K.-M. Lin, Improvement of shape memory effect in Fe-Mn-Si alloy by slight tantalum addition, *Mater. Sci. Eng.: A* 518 (2009) 139–143, <https://doi.org/10.1016/j.msea.2009.04.036>.
- [42] D. Wang, X. Yang, Q. Liao, H. Peng, Y. Wen, Significant improvement of shape memory effect in Co-Ni-based alloys through Si alloying, *J. Alloy. Compd.* 791 (2019) 501–507, <https://doi.org/10.1016/j.jallcom.2019.03.352>.
- [43] M. Koyama, M. Murakami, K. Ogawa, T. Kikuchi, T. Sawaguchi, Influence of Al on shape memory effect and twinning induced plasticity of Fe-Mn-Si-Al system alloy, *J. Jpn. Inst. Met.* 71 (2007) 502–507, <https://doi.org/10.2320/jinstmet.71.502>.
- [44] G. Wang, H. Peng, C. Zhang, S. Wang, Y. Wen, Relationship among grain size, annealing twins and shape memory effect in Fe-Mn-Si based shape memory alloys, *Smart Mater. Struct.* 25 (2016), 075013, <https://doi.org/10.1088/0964-1726/25/7/075013>.
- [45] Q. Liao, T. Jing, Y. Wang, H. Peng, Y. Wen, A CoCrFeNiMnSi high entropy alloy showing a good combination of shape memory effect and mechanical properties, *J. Alloy. Compd.* 926 (2022), 166803, <https://doi.org/10.1016/j.jallcom.2022.166803>.
- [46] M.-M. Pan, X.-M. Zhang, D. Zhou, R.D.K. Misra, P. Chen, X.-B. Su, On the significance of C and Co on shape memory performance of Fe-Mn-Si-Cr-Ni shape memory alloy, *Mater. Sci. Eng.: A* 786 (2020), 139412, <https://doi.org/10.1016/j.msea.2020.139412>.
- [47] M.J. Xue, X.Y. Xue, H. Zhang, J.S. Li, M.J. Lai, Re-examination of the effect of reducing annealing twin boundary density on the shape memory effect in Fe-Mn-Si-based alloys, *J. Alloy. Compd.* 907 (2022), 164505, <https://doi.org/10.1016/j.jallcom.2022.164505>.
- [48] D. Kim, I. Ferretto, J.B. Jeon, C. Leinenbach, W. Lee, Formation of metastable bcc- $\delta$  phase and its transformation to fcc- $\gamma$  in laser powder bed fusion of Fe-Mn-Si shape memory alloy, *J. Mater. Res. Technol.* 14 (2021) 2782–2788, <https://doi.org/10.1016/j.jmrt.2021.08.119>.
- [49] Y.H. Wen, H.B. Peng, P.P. Sun, G. Liu, N. Li, A novel training-free cast Fe-18Mn-5.5Si-9.5Cr-4Ni shape memory alloy with lathy delta ferrite, *Scr. Mater.* 62 (2010) 55–58, <https://doi.org/10.1016/j.scriptamat.2009.10.004>.
- [50] N. Suutala, Effect of manganese and nitrogen on the solidification mode in austenitic stainless steel welds, *Met. Mater. Trans. A* 13 (1982) 2121–2130, <https://doi.org/10.1007/BF02648382>.
- [51] R. Casati, J. Lemke, M. Vedani, Microstructure and fracture behavior of 316L austenitic stainless steel produced by selective laser melting, *J. Mater. Sci. Technol.* 32 (2016) 738–744, <https://doi.org/10.1016/j.jmst.2016.06.016>.
- [52] H. Li, S. Thomas, C. Hutchinson, Delivering microstructural complexity to additively manufactured metals through controlled mesoscale chemical heterogeneity, *Acta Mater.* 226 (2022), 117637, <https://doi.org/10.1016/j.actamat.2022.117637>.
- [53] S. Vunnam, A. Saboo, C. Sudbrack, T.L. Starr, Effect of powder chemical composition on the as-built microstructure of 17-4 PH stainless steel processed by selective laser melting, *Addit. Manuf.* 30 (2019), 100876, <https://doi.org/10.1016/j.addma.2019.100876>.
- [54] M. Alnajjar, F. Christien, K. Wolski, C. Bosch, Evidence of austenite by-passing in a stainless steel obtained from laser melting additive manufacturing, *Addit. Manuf.* 25 (2019) 187–195, <https://doi.org/10.1016/j.addma.2018.11.004>.
- [55] U. Scipioni Bertoli, G. Guss, S. Wu, M.J. Matthews, J.M. Schoenung, In-situ characterization of laser-powder interaction and cooling rates through high-speed imaging of powder bed fusion additive manufacturing, *Mater. Des.* 135 (2017) 385–396, <https://doi.org/10.1016/j.matdes.2017.09.044>.
- [56] J. Günther, F. Brenne, M. Droste, M. Wendler, O. Volkova, H. Biermann, T. Niendorf, Design of novel materials for additive manufacturing - Isotropic microstructure and high defect tolerance, *Sci. Rep.* 8 (2018), 1298, <https://doi.org/10.1038/s41598-018-19376-0>.
- [57] D. Kim, I. Ferretto, W. Kim, C. Leinenbach, W. Lee, Effect of post-heat treatment conditions on shape memory property in 4D printed Fe-17Mn-5Si-10Cr-4Ni shape memory alloy, *Mater. Sci. Eng.: A* 852 (2022), 143689, <https://doi.org/10.1016/j.msea.2022.143689>.
- [58] J. Günther, R. Lehnert, R. Wagner, C. Burkhardt, M. Wendler, O. Volkova, H. Biermann, T. Niendorf, Effect of compositional variation induced by EBM processing on deformation behavior and phase stability of austenitic Cr-Mn-Ni TRIP steel, *JOM* 72 (2020) 1052–1064, <https://doi.org/10.1007/s11837-020-04018-6>.
- [59] J. Liu, P. Wen, Metal vaporization and its influence during laser powder bed fusion process, *Mater. Des.* 215 (2022), 110505, <https://doi.org/10.1016/j.matdes.2022.110505>.
- [60] H. Jiang, X. Wang, R. Xi, G. Li, H. Wei, J. Liu, B. Zhang, S. Kustov, K. Vanmeensel, J. Van Humbeeck, G. Zhao, Size effect on the microstructure, phase transformation behavior, and mechanical properties of NiTi shape memory alloys fabricated by laser powder bed fusion, *J. Mater. Sci. Technol.* 157 (2023) 200–212, <https://doi.org/10.1016/j.jmst.2023.02.026>.
- [61] S.B. Tate, S. Liu, Solidification behaviour of laser welded type 21Cr-6Ni-9Mn stainless steel, *Sci. Technol. Weld. Join.* 19 (2014) 310–317, <https://doi.org/10.1179/1362171813Y.0000000189>.
- [62] H. Peng, Y. Wen, Y. Du, J. Chen, Q. Yang, A New Set of Creq and Nieg equations for predicting solidification modes of cast austenitic Fe-Mn-Si-Cr-Ni shape memory alloys, *Met. Mater. Trans. B* 45 (2014) 6–11, <https://doi.org/10.1007/s11663-013-0005-8>.
- [63] M. Wendler, J. Mola, L. Krüger, A. Weiß, Experimental quantification of the austenite-stabilizing effect of Mn in CrMnNi As-cast stainless steels, *Steel Res. Int.* 85 (2014) 803–810, <https://doi.org/10.1002/srin.201300271>.
- [64] T.J. Lienert, J.C. Lippold, Improved weldability diagram for pulsed laser welded austenitic stainless steels, *Sci. Technol. Weld. Join.* 8 (2003) 1–9, <https://doi.org/10.1179/136217103225008847>.
- [65] S.A. David, J.M. Vitek, R.W. Reed, T.L. Hebble, Effect of rapid solidification on stainless steel weld metal microstructures and its implications on the Schaeffler diagram, Oak Ridge National Lab. (ORNL), Oak Ridge, TN (United States), 1987, <https://doi.org/10.2172/5957599>.
- [66] M. Wendler, A. Weiß, L. Krüger, J. Mola, A. Franke, A. Kovalev, S. Wolf, Effect of manganese on microstructure and mechanical properties of cast high alloyed CrMnNi-N steels, *Adv. Eng. Mater.* 15 (2013) 558–565, <https://doi.org/10.1002/adem.201200318>.
- [67] S. Shrestha, K. Chou, Residual heat effect on the melt pool geometry during the laser powder bed fusion process, *J. Manuf. Mater. Process.* 6 (2022) 153, <https://doi.org/10.3390/jmmp6060153>.
- [68] W.E. King, H.D. Barth, V.M. Castillo, G.F. Gallegos, J.W. Gibbs, D.E. Hahn, C. Kamath, A.M. Rubenchik, Observation of keyhole-mode laser melting in laser powder-bed fusion additive manufacturing, *J. Mater. Process. Technol.* 214 (2014) 2915–2925, <https://doi.org/10.1016/j.jmatprotec.2014.06.005>.
- [69] D. Bergström, J. Powell, A.F.H. Kaplan, The absorbance of steels to Nd:YLF and Nd:YAG laser light at room temperature, *Appl. Surf. Sci.* 253 (2007) 5017–5028, <https://doi.org/10.1016/j.apsusc.2006.11.018>.
- [70] A.F.H. Kaplan, Local absorptivity modulation of a 1 $\mu$ m-laser beam through surface waviness, *Appl. Surf. Sci.* 258 (2012) 9732–9736, <https://doi.org/10.1016/j.apsusc.2012.06.020>.
- [71] J. Xie, A. Kar, Laser Welding of Thin Sheet Steel with Surface Oxidation, (n.d.) 6.
- [72] L.K. Ang, Y.Y. Lau, R.M. Gilgenbach, H.L. Spindler, Analysis of laser absorption on a rough metal surface, *Appl. Phys. Lett.* 70 (1997) 696–698, <https://doi.org/10.1063/1.118242>.
- [73] N.K. Tolochko, Y.V. Khlopkov, S.E. Mozzharov, M.B. Ignatiev, T. Laoui, V.I. Titov, Absorbance of powder materials suitable for laser sintering, *Rapid Prototyp. J.* 6 (2000) 155–161, <https://doi.org/10.1108/13552540010337029>.
- [74] J.W. Elmer, The influence of cooling rate on the microstructure of stainless steel alloys, Lawrence Livermore National Lab., CA (USA), 1988, <https://doi.org/10.2172/5678406>.
- [75] W. Liu, J. Ma, M.M. Atabaki, R. Pillai, B. Kumar, U. Vasudevan, H. Sreshta, R. Kovacevic, Hybrid laser-arc welding of 17-4 PH martensitic stainless steel, *Lasers Manuf. Mater. Process.* 2 (2015) 74–90, <https://doi.org/10.1007/s40516-015-0007-2>.
- [76] K. Poorhaydari, B.M. Patchett, D.G. Ivey, Estimation of Cooling Rate in the Welding of Plates with Intermediate Thickness, (n.d.) 7.
- [77] C.R. Das, H.C. Dey, G. Srinivasan, S.K. Albert, A.K. Bhaduri, A. Dasgupta, Weldability of 17-4PH stainless steel in overaged heat treated condition, *Sci. Technol. Weld. Join.* 11 (2006) 502–508, <https://doi.org/10.1179/174329306X148147>.
- [78] M.S. Moyle, N. Haghdadi, X.Z. Liao, S.P. Ringer, S. Primig, On the microstructure and texture evolution in 17-4 PH stainless steel during laser powder bed fusion: Towards textural design, *J. Mater. Sci. Technol.* 117 (2022) 183–195, <https://doi.org/10.1016/j.jmst.2021.12.015>.
- [79] X. Miao, M. Wu, J. Han, H. Li, X. Ye, Effect of laser rescanning on the characteristics and residual stress of selective laser melted titanium Ti6Al4V alloy, *Mater. (Basel)* 13 (2020) 3940, <https://doi.org/10.3390/ma13183940>.
- [80] Y. Wang, M. Chen, F. Zhou, E. Ma, High tensile ductility in a nanostructured metal, *Nature* 419 (2002) 912–915, <https://doi.org/10.1038/nature01133>.
- [81] X. Wu, M. Yang, F. Yuan, G. Wu, Y. Wei, X. Huang, Y. Zhu, Heterogeneous lamella structure unites ultrafine-grain strength with coarse-grain ductility, *Proc. Natl. Acad. Sci. USA* 112 (2015) 14501–14505, <https://doi.org/10.1073/pnas.1517193112>.
- [82] P.V. Mutterle, M. Zendron, M. Perina, A. Molinari INFLUENCE OF DELTA FERRITE ON MECHANICAL PROPERTIES OF STAINLESS STEEL PRODUCED BY MIM, (n.d.) 6.
- [83] K.R. Gadelrab, G. Li, M. Chiesa, T. Souier, Local characterization of austenite and ferrite phases in duplex stainless steel using MFM and nanoindentation, *J. Mater. Res.* 27 (2012) 1573–1579, <https://doi.org/10.1557/jmr.2012.99>.
- [84] R.B. Figueiredo, T.G. Langdon, Effect of grain size on strength and strain rate sensitivity in metals, *J. Mater. Sci.* 57 (2022) 5210–5229, <https://doi.org/10.1007/s10853-022-06919-0>.
- [85] M.J. Lai, Y.J. Li, L. Lillpopp, D. Ponge, S. Will, D. Raabe, On the origin of the improvement of shape memory effect by precipitating VC in Fe-Mn-Si-based shape memory alloys, *Acta Materialia* 155 (n.d.) 222–235.
- [86] S. Kajiura, Characteristic features of shape memory effect and related transformation behavior in Fe-based alloys, *Mater. Sci. Eng.: A* 273–275 (1999) 67–88, [https://doi.org/10.1016/S0921-5093\(99\)00290-7](https://doi.org/10.1016/S0921-5093(99)00290-7).
- [87] E. Demir, D. Raabe, N. Zaafarani, S. Zaefferer, Investigation of the indentation size effect through the measurement of the geometrically necessary dislocations beneath small indents of different depths using EBSD tomography, *Acta Mater.* 57 (2009) 559–569, <https://doi.org/10.1016/j.actamat.2008.09.039>.
- [88] C. Tan, Y. Chew, R. Duan, F. Weng, S. Sui, F.L. Ng, Z. Du, G. Bi, Additive manufacturing of multi-scale heterostructured high-strength steels, *Mater. Res. Lett.* 9 (2021) 291–299, <https://doi.org/10.1080/21663831.2021.1904299>.
- [89] X.T. Fang, G.Z. He, C. Zheng, X.L. Ma, D. Kaoumi, Y.S. Li, Y.T. Zhu, Effect of heterostructure and hetero-deformation induced hardening on the strength and ductility of brass, *Acta Mater.* 186 (2020) 644–655, <https://doi.org/10.1016/j.actamat.2020.01.037>.

- [90] C. Tan, Y. Liu, F. Weng, F.L. Ng, J. Su, Z. Xu, X.D. Ngai, Y. Chew, Additive manufacturing of voxelized heterostructured materials with hierarchical phases, *Addit. Manuf.* 54 (2022), 102775, <https://doi.org/10.1016/j.addma.2022.102775>.
- [91] W. Lee, B. Weber, G. Feltrin, C. Czaderski, M. Motavalli, C. Leinenbach, Stress recovery behaviour of an Fe-Mn-Si-Cr-Ni-VC shape memory alloy used for prestressing, *Smart Mater. Struct.* 22 (2013) 5037, <https://doi.org/10.1088/0964-1726/22/12/125037>.
- [92] M. Schuster, A. De Luca, D. Kucajda, E. Hosseini, R. Widmer, X. Maeder, C. Leinenbach, Heat treatment response and mechanical properties of a Zr-modified AA2618 aluminum alloy fabricated by laser powder bed fusion, *J. Alloy. Compd.* 962 (2023), 171166, <https://doi.org/10.1016/j.jallcom.2023.171166>.
- [93] F.H. Kim, S.P. Moylan, T.Q. Phan, E.J. Garboczi, Investigation of the effect of artificial internal defects on the tensile behavior of laser powder bed fusion 17–4 stainless steel samples: simultaneous tensile testing and X-ray computed tomography, *Exp. Mech.* 60 (2020) 987–1004, <https://doi.org/10.1007/s11340-020-00604-6>.